Bachelor Thesis

Investigation of the radiation error and heat transport at the snow-air interface using fibre-optic distributed sensing during the polar night in Adventdalen, Svalbard

Felix Roland Heuring

Student number: 1686320

Supervised by

Prof. Dr. Christoph Thomas

Dr. Wolfgang Babel

Bayreuth, April 2023

Abstract

Measured or estimated values of the insulating properties of snow are utilized in a variety of fields, including planetary geophysics, climate modelling, and glaciology. Investigation on permafrost or ground freezing makes an accurate determination of the thermal conductivity of the snow cover indispensable. Furthermore, a more accurate determination of this thermodynamic property would improve our knowledge with key hydrological phenomena such as snow melt or heat and water vapor exchange with the atmosphere and could help understand the mechanisms of artic amplification. To sufficiently understand the surface heat transport in northern regions and glacier zones, we still need to explore the role of near surface turbulence in the exchange of energy within the snow-air continuum. Previous research has identified wind pumping as a mechanism that stimulates snow sublimation on the surface at high frequencies and generates air flow into the firn at lower frequencies. This research suggests that the theoretical predictions for perturbation pressure attenuation with depth in the top layer of snowpack at high frequencies are lower than what is observed. As a result, the potential for enhanced sublimation will occur over a shallower depth of snow. It was shown that the variation of the boundary layer pressure field drives near-surface circulation inside the snow volume.

The objective of the measurement campaign in Svalbard was to enhance the current observations of this process by integrating traditional observing methods with a sophisticated use of the innovative fiber-optic distributed sensing (FODS) method. This technique enables continuous observations in both temporal and spatial dimensions. The targeted research questions of this thesis were: (1) what influence has the usage of various types of optical fibre on the measurement of air and snow temperatures as result of a potential longwave radiation error during the polar night? (2) How does the heat diffusivity inside the snow respond to turbulence in the overlying surface layer? Research into these questions aims to prove/disprove the two hypotheses. Firstly, that a greater diameter at 0/8 cloudiness leads to a negative ΔT in comparison to the fibre with smaller diameter, caused by the significant radiation error over a cold surface and secondly, that the heat diffusivity increases in phases of high TKE through forced induction of air in the porous snow medium.

(1) A model was created to determine the importance of the error via radiative forcing, by calculating an energy balance around the boundaries of a coiled DTS system. The FO column utilizes a support structure with a helically coiled fiber-optic cable to address the limitation of along-fiber resolution of the DTS instrument and enhance the spatial resolution to the millimetre scale in one dimension. The energy balance model accounts for the longwave radiation balance, the transfer of heat through forced convection, and the conduction term at the point where the system is in contact with the support structure. The versatility of this model allows it to be utilized under a range of meteorological conditions or with different material properties, making it an adjustable tool for evaluating the effectiveness of the coiled DTS system. Its application to the dataset, collected during the polar night 2022, yielded an estimation of the expected temperature difference between FODS temperatures and the dry-bulb air temperature. This approach shows, that measuring with a 900 μm PVC coated FO cable, causes an increased radiation error compared to a thinner, 250 μm thick, clear-coated FO cable. Under the observed conditions a maximum deviation between the two fibers of 0.1 K occurred. In comparison to the Bias of the Silixa XT, which was determined as 0.03 K, in this setup allows the conclusion, that a correction of the FODS data can be sensible to ensure a consistently high precision.

(2) To observe the correlation of TKE (m^2s^{-2}), means the kinetic energy per unit mass associated with eddies in the turbulent flow, and the heat transfer detailed information about the trend of the thermodynamic properties of the snow volume were necessary. To accomplish this, a numerical method, known as Euler implicit, was utilized to solve the heat equation (9) in both time and space, using a variety of diffusivity values. Through a series of iterations, the range of effective thermal

diffusivities was narrowed down to minimize the discrepancy between measured temperatures and predicted temperatures, as measured by the root mean square error. To obtain a high accuracy for the calculation, a snow height detection was implemented providing detailed information about the snow depth at the sampling side. Otherwise, the determined low-frequency trend of the heat diffusivity may have been influenced by the fluctuations of the snow height. The results of the thermodynamic properties were decomposed into different frequency levels by use of the Bior 5.5 wavelet library. The Bior 5.5 is a biorthogonal two-channel wavelet filter bank, that allows for a time-frequency analysis of the signal, meaning that it can identify patterns that occur at specific times and frequencies. A comparison between the TKE and the low-frequency decomposition showed an anticorrelated trend and therefore refuted the preceded hypothesis. Although in summary the heat equation could be solved successfully with the FODS data, obtaining high resolution reproduction of the thermodynamics inside an artic snow layer, an explanation for the anticorrelated trend of α and TKE stays unsolved and should be objective for further research.

Zusammenfassung

Die thermodynamischen Eigenschaften von Schnee, gemessen oder geschätzt, finden in verschiedensten Bereichen der Umweltforschung eine Anwendung, in der planetaren Geophysik, in Klimamodellen, aber auch ganz entscheidend in der Kryosphärenwissenschaft und Glaziologie. Untersuchungen zu Permafrost oder allgemeinem Bodenfrost erfordern eine genaue Bestimmung der Wärmeleitfähigkeit der Schneedecke. Für eine aussagekräftige Vorhersage über hydrologische Phänomene, wie Schneeschmelze oder den Austausch von Wärme und Wasserdampf mit der Atmosphäre, ist die Kenntnis zu der isolierenden Beschaffenheit des Schnees unerlässlich. Dies ist nicht zuletzt ein fundamentaler Aspekt im Kontext der polaren Verstärkung. Um den Wärmetransport an der Oberfläche in nördlichen Regionen und Gletscherzonen ausreichend zu verstehen, müssen wir die Rolle der turbulenten Austauschprozesse zwischen Schnee und Luft in der Nähe der Oberfläche untersuchen. Frühere Untersuchungen haben „Windpumpen" als Mechanismus identifiziert, der die Sublimation von Schnee an der Oberfläche bei hohen Frequenzen stimuliert und bei niedrigeren Frequenzen einen Luftstrom in den Firn erzeugt. Die Forschung legt nahe, dass theoretische Vorhersagen für die Dämpfung des Stördrucks mit der Tiefe in der oberen Schneedecke bei hohen Frequenzen niedriger sind als das, was beobachtet werden konnte. Dadurch wird das Potenzial für verstärkte Sublimation in geringerer Schneetiefe auftreten. Es konnte gezeigt werden, dass die Variation des Druckfeldes in der Grenzschicht eine Zirkulation nahe der Oberfläche innerhalb des Schneekörpers erzeugt.

Das Ziel der Messkampagne auf Svalbard war es, den derzeitigen Forschungsstand dieses Prozesses durch die Integration traditioneller Beobachtungsmethoden in Kombination mit der innovativen FODS-Methode zu verbessern. Diese Technik ermöglicht kontinuierliche Beobachtungen in sowohl zeitlicher als auch räumlicher Dimension. Der Inhalt dieser Forschungsarbeit widmet sich folgenden Forschungsfragen: (1) In welcher Amplitude bewegen sich die auftretenden Messabweichungen auf FODS-Sensoren je nach Fehlerquelle während der Polarnacht und (2) welche Korrelation ergibt sich aus dem Trend der Wärmediffusivität innerhalb einer arktischen Schneemasse und der näheren Turbulenz an der darüberliegenden Grenzfläche. Die Forschung zu diesen Fragen zielt darauf ab, die folgenden Arbeitshypothesen zu beweisen bzw. zu widerlegen. Erstens, dass ein größerer Durchmesser bei 0/8 Bewölkungsanteil zu einem negativen ΔT im Vergleich zu einer Faser mit kleinerem Durchmesser führt, verursacht durch den signifikanten Strahlungsfehler über einer kalten Oberfläche. Sowie zweitens, dass die Wärmediffusivität in Phasen mit hoher kinetischer Energie der Turbulenzen durch die erzwungene Konvektion von Luft in den porösen Schnee zunimmt.

(1) Um die Bedeutung des Fehlers durch den Strahlungsantrieb zu bestimmen, wurde ein Energiebilanzmodel um die imaginären Grenzen des gewickelten DTS-Systems entwickelt. Die optische Glasfasersäule verwendet eine Stützstruktur mit einer gewundenen Glasfaserhelix, um die Einschränkung der Auflösung entlang der Faser durch das DTS-Instruments zu überwinden und die räumliche Auflösung in einer Dimension auf den Millimeterbereich zu erhöhen. Das Model berücksichtigt die langwellige Strahlungsbilanz, den Wärmetransport durch erzwungene Konvektion und den Leitungsterm an den Kontaktstellen des Systems mit der Trägerstruktur. Die Vielseitigkeit dieses Modells ermöglicht den Einsatz unter einer Reihe von meteorologischen Bedingungen oder mit unterschiedlichen Materialeigenschaften und macht es zu einem anpassungsfähigen Werkzeug zur Bewertung der Genauigkeit des DTS-Systems. Die Anwendung auf den Datensatz, der während der Polarnacht 2022 gesammelt wurde, lieferte die erwartete Abweichung zwischen den FODS-Temperaturen und der tatsächlichen Temperatur. Das Modell zeigt, dass Messungen mit einem 900 µm dicken PVC-beschichteten FO-Kabel einen höheren Fehler verursachen als mit einem dünneren, 250 µm starken, klar beschichteten optischen Glasfaserkabel. Unter den gemessenen vorherrschenden Bedingungen verursachten der Strahlungshaushalt und die Strömungsregime eine maximale Abweichung von 0.1 K zwischen den beiden Fasertypen. Der Vergleich mit dem Bias des Messgerätes Silixa XT (0.03 K) führt zu dem Schluss, dass eine Korrektur der FODS-Daten im Hinblick auf eine möglichst hohe Präzision vorgenommen werden sollte oder die dünnere Faser verwendet werden sollte, wenn die Ansprüche an Zugfestigkeit und Robustheit es zulassen.

(2) Um eine Korrelation zwischen der TKE (m^2s^{-2}), also der Energie, die pro Masseeinheit in Wirbeln enthalten ist und dem Wärmeaustausch herzustellen, waren detaillierte Informationen über den Trend der thermodynamischen Eigenschaften des Schneevolumens notwendig. Um dies zu erreichen, wurde das implizite Euler Verfahren eingesetzt, um die Wärmeleitungsgleichung, in der Zeit als auch Raum, unter Verwendung verschiedener Werte für die Wärmediffusivität zu lösen. Durch eine Reihe von Iterationen wurde der Bereich der effektiven thermischen Diffusivität eingegrenzt, um den Unterschied zwischen gemessenen und vorhergesagten Temperaturen zu minimieren, wie durch den Root Mean Square Error gemessen. Um eine hohe Genauigkeit der Berechnung zu erreichen, wurde eine Schneehöhenerkennung implementiert, die detaillierte Informationen über die Schneeverteilung auf der Messsäule lieferte. Andernfalls hätte die Bestimmung der Wärmeleitfähigkeit durch die Fluktuationen der Schneehöhe beeinflusst werden können. Die Ergebnisse der thermodynamischen Eigenschaften wurden mithilfe der Bior5.5 Wavelet-Bibliothek in unterschiedliche Frequenzbereiche zerlegt. Bior 5.5 ist eine bi-orthogonales Wavelet-Filterbank, die eine Zeit-Frequenz-Analyse des Signals ermöglicht, d.h. es können Muster identifiziert werden, die zu bestimmten Zeiten und Frequenzen auftreten. Ein Vergleich zwischen TKE und der Niedrigfrequenzzerlegung zeigte einen antikorrelierten Trend und widerlegte somit die aufgestellte Hypothese. Zusammenfassend konnte die Wärmegleichung mit den FODS-Daten erfolgreich gelöst werden, wobei ein hochauflösendes Bild der Thermodynamik innerhalb der arktischen Schneeschicht generiert werden konnte. Dennoch bleibt eine Erklärung für den antikorrelierten Trend von α und TKE ausstehend und sollte Gegenstand für weitere Forschung sein.

Contents

List of figures

List of abbreviations

List of tables

List of symbols

symbol	explanation	unit
c_f	Specific heat capacity of a fiber-optic cable	(J kg^{-1} K^{-1})
c_p	Specific heat capacity of air	(J kg^{-1} K^{-1})
C	Dimensionless parameter	(-)
D_c	Critical event duration	(s)
P	Power	(W)
g	Gravitational acceleration	(m s^{-2})
I $\downarrow$	Incoming longwave radiation	(W m^{-2})
I $\uparrow$	Outgoing longwave radiation	(W m^{-2})
K $\downarrow$	Incoming shortwave radiation	(W m^{-2})
K $\uparrow$	Shortwave reflex radiation	(W m^{-2})
K_a	Thermal conductivity of air	(W m^{-1} K^{-1})
LAF	Length along the fiber	(m)
n	Dimensionless parameter	(-)
p	Atmospheric pressure	(Pa)
Pr	Prandtl number	(-)
Q_{cond}	Specific conductive heat flux	(W m^{-2})
Q_{conv}	Specific convective heat flux	(W m^{-2})
Q_E	Latent heat flux	(W m^{-2})
Q_G	Ground heat flux	(W m^{-2})
Q_H	Sensible heat flux	(W m^{-2})
Q	Net radiation	(W m^{-2})
Q_S	Storage term	(W m^{-2})
R_a	Specific gas constant	(J kg^{-1} K^{-1})
Re	Reynolds number	(-)
r	Radius	(m)
t	Time	(s)
T	Temperature	(K or °C)
T_{Af}	FO temperature, with error correction in air application	(K)
T_A	Dry-bulb air temperature	
T_f	Temperature of the fiber-optic cable	(K)
T_s	Sonic temperature	(K or °C)
TKE	Turbulent kinetic energy	(m^2 s^{-2})
U	Wind speed	(m s^{-1})
u	Wind component from east to west	(m s^{-1})
u*	Friction velocity	(m s^{-1})
V	Volume	(m^3)
v	Wind component from south to north	(m s^{-1})
v_a	Kinematic viscosity of air	(m^2 s^{-1})
z	Height above ground	(m)
Δ	Difference	(-)
ϵ_s	Surface emissivity	(-)
π	Ratio of a circle's circumference to its diameter	(-)
ρ	Density	(Kg m^{-3})
σ	Standard deviation	(-)
σ^2	Variance	(-)
σ_S	Stefan-Boltzmann constant	(W m^{-2} K^{-4})
υ_A	Kinematic viscosity of air	(m^2 s^{-1})

1. Introduction

Human life changes the composition of our atmosphere. Due to the anthropogenic emissions of greenhouse gases, the net radiation balance of our planet changes, causing an increase of the global temperature. Especially at the poles the temperature rise is larger compared to the planetary average, a phenomenon commonly referred to as artic amplification (Vihma, 2011). Polar regions are characterized by a variety of sharp transition between different surface types, for example, sea and ice or snow and rocks, which differ drastically in their properties, like roughness, albedo and thermal properties (van den Broeke et al., 2011). This eventually causes large gradients in proximity. The balancing of the energy gradients results in enhance the heat transfer and thus be a reason for polar amplification. Understanding heat transfer in polar environment therefore will be an essential objective for upcoming geophysical research. Measured or estimated values of the insulating properties of snow are used in a wide range of studies including planetary geophysics, climate modelling and glaciology. In studies of permafrost or ground freezing, an accurate determination of the thermal conductivity of the snow cover is indispensable (Sturm et al., 1997). Since heat conductivity of ice exceeds the conductivity of the air by two orders of magnitude, snow, as two-phase complex, shows a broad range in its thermodynamic properties, cause its structure varies with aspects, like precipitation or temperature. Furthermore, the air-filled pore volume plays an important role. The influence of the pore space on the heat diffusivity is still a big research gaps for understanding surface heat transport in northern regions and glacier zones. Equally a more accurate determination of this thermodynamic property could give deeper insights to key hydrological phenomena like snow melt, heat transfer and water respectively vapor exchange with the atmosphere (Oldroyd et al., 2013). Distributed sensing technologies may play a key role during this process by filling the gap between single point measurements and remote sensing technologies, providing an enhanced temporal and spatial resolution over classic measurement methods. (Foken, 2021).

FODS has found its way into geosciences in the last decade. While in the original sense the technique was developed for measuring temperature, the current portfolio has extended to other basic meteorology units, such as solar radiation, air humidity, wind speed and soil moisture. FODS collects thousands of measurements at high resolution scales along a fiber-optic cable. At the same time, it provides data at sampling rates of up to 1 Hz over distances to several kilometres (Thomas et al., 2012). This property enables a rapid evolution of the existing possibilities to an expanded range of applications in surface and boundary-layer meteorology. New applications include vertical and horizontal profiling, investigating the spatial structure of turbulence and resolving the response of airflow to land-surface heterogeneity. The ability of a single optical fibre to observe across a variety of media, such as air, mineral soil, plant tissue, ice, water and at least snow, is a unique strength of FODS against many other remote sensing techniques and lends itself to interdisciplinary geosciences research (Thomas and Selker, 2021). The last mentioned application has been examined during the NYTEFOX campaign (Zeller et al., 2021). Despite some issue with the emissivity of the selected materials, FODS have proven its capability for the cold and rough enviroment at 79° northern latidude. DTS contributes not only to advanced capabilities in the field of meteorology, but also in other disciplines of environmental siences. Because of its high precision, FODS in hydrology allows for precisely locating the groundwater sources inside the hyporheic zone of a receiving water by temperatures variabilty (Drusová et al., 2021). Furthermore the quality of geo-chemical models can be enhanced with the temperature data with its high spatial and temporal resolution (Selker et al., 2006).

The capability of measuring wind speed by the use of paired passive and actively heated fiber optic sensor, similar to the concept of a hot wired anemometer, was examined in earlier investigations (Sayde et al., 2015). Wind speeds can be determined by the relation of energy loss from a heated

surface with the heat transfer coefficient, which in turn is dependent on the forced convection of the air stream over the fibre (Freundorfer et al., 2021). While this area of application brings the convective heat transfer about intentionally to utilize it for airflow and windspeed observations, during investigations of the dry-bulb air temperature convection can be an unwished error source, misrepresenting the result of the actual measurement. Forced convection influences essentially the results on air temperature measurements as to be observed as one major measurement error during the first research question. The geometry of the FO cable is a critical factor for the energy transfer via convection, thus the variation in the FO cable needs to be a subject of research. There is still a knowledge gap, about the actual effect measuring in situ with differing FO fibre properties.

Any deviation in the measured temperature is based on a difference of the internal kinetic energy between the sensor and the observed media. According to thermodynamics, the transfer of energy can either be enabled by heat conduction in direct contact, heat convection through the overflow of a fluid or radiation (Žkauskas, 1987). By employing an energy balance approach these fundamental principles are considered and the caused measurement error could be validated. Mathematically expressed, the energy balance can be described as the change rate of internal energy E (J) stored in a FO cable segment.

$$\frac{\partial E}{\partial t} = c_p \, \rho \, V \, \frac{\partial T}{\partial t}$$

$$(\; 1 \;)$$

where cp, (J kg^{-1} K^{-1}) is the FO cables specific heat capacity, ρ (kg m^{-3}) the FO cables density, V (m^3) is the volume of the FO cable segment, T (K) is the FO cable segment temperature, t (s) is the time, see also Equation (1). The surface energy balance of the fibre is one universal characteristic, when comparing two fibre types, cause of variating heat transfer coefficient and radiation properties (Sayde et al., 2015).

1.1. Radiation error (RQ1)

When examining small-scale processes, for example the dynamics of cold air flow during night-time or the thermodynamics inside a snow volume at the end of polar night, it may be necessary to use a more precise spatial resolution than what can be obtained with a straight fiber-optic cable (Sigmund et al., 2017). This is due to the limited along-fiber resolution of the DTS instrument, which typically only allows for resolution on the order of several tens of centimetres. To address this limitation, some studies have employed a support structure that coils the fiber-optic cable in a helical pattern, which enhances the spatial resolution to the millimetre scale in one dimension. Our application required precise vertical temperature profiles for the snow-air continuum, that extended 1.5 m in height. To achieve this, the coiled-fiber-optic approach was utilized. Related to this field observation the resolution along the axis of the FO cable was 0.25 m. Through the coiling around a column of reinforcement fiber with 1.0 m circumference, the vertical resolution was reduced to $dz =$ 0.00254 m, by assuming the horizontal cross-section of the column to be homogeneous. However, previous studies have identified two important issues with this method. The first issue arises when the fiber cable is coiled around a support structure with a very small diameter (less than 3.2 cm) (Arnon et al., 2014). This can cause temperature artifacts at the beginning of the coil due to significant differential attenuation caused by the strong bending. This issue was eliminated by choosing a diameter of d = 0.31 m for the FO column. The second issue involves radiative heating and/ or cooling of the coiled fiber-optic cable and support structure, which can result in substantial radiation errors of several Kelvin, particularly in aerial applications (Sigmund et al., 2017). The error during polar night for a coiled DTS system is comprised of both the direct effect of radiative transfer to and from the fiber cable, as well as the indirect effect of the support structure via heat conduction. Last mentioned error through

heat conduction was found as insignificant over the influence of radiative transfer (Sigmund et al., 2017). The validation of longwave error gets the main focus in this research question. The first objective of this thesis is focused on a comparison of two FO cable types and their systematic error through longwave radiative transfer based on the gained FODS data from this field campaign. The setup, including the two different kinds of fibre, serves the purpose to determine the longwave radiation error in dependence of the fibre geometry based on both vertical temperature profiles.

The following hypothesis should be verified to answer this research question: A greater diameter at 0/8 cloudiness leads to a negative ΔT in comparison to the fibre with smaller diameter, caused by the significant radiation error over a cold surface.

1.2. Heat transport (RQ2)

Previous research assesses the small temporal and spatial resolution of classic measurement methods as the main limitation of the calculation of the heat diffusivity and thus for the thermal conductivity. As conclusion of an experiment in 2012, the high spatial and temporal resolution (2.5/10 cm in 1 min) measured by thermocouples proves, that lower sampling resolution leads to a strong overestimation of the diffusivity (Oldroyd et al., 2013). While fibre-optic distributed sensing (FODS) raised the technical and economical feasible resolution of temperature measurements in space as well as in time, this leads to interesting question, whether the determination of thermal diffusivity could be approached easier and even more accurately with the helically coiled FO column, which was presented in the previous chapter.

A profound knowledge about the process of heat transfer between surface and atmosphere in the artic regions is one fundamental aspect to solve the backgrounds of artic amplification. Next to the well-researched physical process of heat conduction inside solids, there is still a huge research gap at the processes of two-phase and porous media. Especially, when it comes to measurement in-situ, the current state of research is insufficiently and the role of near surface turbulence in the exchange of energy within the snow-air continuum is not understood yet. With the current climate there are no thawing events during the winter months on Svalbard and the cold temperatures causing harsh ice crystals, while the low roughness of the surface increases wind induced snow drifts (Singh, 2011). For the heat exchange between surface and the atmosphere, the heat conductivity is not the only determining factor. During observation in Switzerland 2010 wind pumping has been discovered as a process, which drives sublimation of snow on the surface at high forcing frequencies and as a generator for air movement into the firn with lower frequencies. Research suggests, that theoretical predictions suffer from underestimation of the attenuation of the pressure with depth of the snow volume caused by high-frequency perturbation and furthermore the discrepancy of measurements and theory increases with the frequency of pressure gradient (DRAKE et al., 2016). Another conclusion of the research is, that perturbation pressure attenuation is not only dependent on the wind properties and permeability, but instead it is strongly affected by the layering, tortuosity and the hardness of the surface (DRAKE et al., 2016).

Considering this knowledge, the air exchange through turbulence must be taken into account at the quantification of the heat transport inside a porous snowpack. This objective aims to solve the connection between the atmosphere regime and the effective thermodynamic inside an artic snowpack. Therefore, the high spatial and temporal resolution data provided by FODS are used to determine heat diffusivity in the snow layer. The research question is whether, respectively how strong, is the effect of turbulence in the boundary layer flow field on heat diffusivity within the snow. Current knowledge suggests that heat exchange between snow and air is not only driven by heat conduction but also by air movement, which enhances energy transfer by forcing air into the porous medium, thus in theory the turbulence data should show a correlation to the heat diffusivity. To

determine these rather complex mechanisms, this thesis tested a second hypothesis: The heat diffusivity increases in phases of high TKE through forced induction of air in the porous snow medium.

This thesis proposal evolved from the collected data during the AGF350-850 course, which was hold at the UNIS in Longyearbyen 2022. This project served the purpose to educate Master and Ph.D. students to manage a field work campaign in the challenging environment of the artic regions. Through theoretical lectures in advance, new measurement methods were introduced to the students as preparation for the field work. For the first time of this course Prof. Thomas was asked to teach the FODS in situ on the remote archipelago Svalbard. Cause of my employment as research assistant at the department of micrometeorology of the University of Bayreuth, I was able to accompany Prof. Thomas during the class at the end of polar night in February 2022.

2. Methods

This section is structured chronologically and follows the progress of the field campaign. First detailed information about FODS and the location of the field project, including geopolitical, orographic, and climatic characteristics, are given. It continues describing the experimental setup and its implementation. The chapter closes with the data analysis.

FODS can be reduced to four fundamental measurement principles: Raman backscatter, based on the temperature dependency of the backscattered anti-Stokes, Brillouin backscatter, Rayleigh backscatter and Bragg gratings (Thomas and Selker, 2021). Previous research to fibre-optic sensors is limited to the advantages of each fundamental measurement principles. While the Raman backscatter is mostly chosen because of its outstanding accuracy in comparison to measurements with fibre Bragg gratings and continuous fibre Bragg grating, given by the continuous calibration with PT100 probes, the research does not treat a variation and properties of the sensor, i.e., the fiber-optic cable, itself (Drusová et al., 2021). There is hardly any scientific work, which is focused on the type of FO cable, used for the measurement and neither on the variation of resulting data. This might be caused by the fact, that for many purposes in environmental sciences the reaction time of the sensor falls below the timescales of the measurement environment by far, for example soil science. Also, many FO cable types are eliminated by the physical stress, which occurs with the measurement setup itself. However, in the atmosphere temporal resolution of near-surface turbulence can be quite small, which increases the need of a fibre with a small time constant. Furthermore, the radiative transfer between the atmosphere and the fibre radiation plays an important role for meteorological measurements. FODS sensors have various outer shells and therefore differ in the albedo or the absorption of shortwave radiation. This might not be an important factor for soil or most hydrological measurements, but rather significant during aerial applications.

Distributed temperature sensing is an optical measurement method. The determination of temperature alongside an optical fibre, functioning as a linear sensor, is based on the Raman scattering. The local physical dimensions, such as temperature or pressure and tensile forces, affect the glass fibre and change their characteristics of light transmission. The principle behind DTS is, that a laser pulse is emitted into the fibre-optic cable and through the incident the photons are backscattered with a different level of energy (Figure 1). Most photons will be reflected at the wavelength of the original pulse, but a very small part of the energy will be absorbed and re-emitted at shorter and longer wavelengths. These frequency-shifted, i.e., inelastic reflections are called Raman-backscatter. The relationship between the intensities at the Stokes and the Anti-stokes bands indicates the temperature of the glass where the backscatter occurred. The reflection with the longer wavelength is referred to as Stokes backscatter and has a temperature-independent amplitude. The reflection with the shorter wavelength is called Anti-Stokes backscatter and has an amplitude, which non-linearly depends on temperature. By measuring the Stokes/Anti-Stokes ratio, one can measure the temperature everywhere along the cable, see Equation (2) (Thomas and Selker, 2021). Optical-fibre-based distributed sensing (OFDS) enables a wide range of exciting applications in surface and boundary-layer meteorology, including vertical and horizontal profiling, investigating the spatial structure of the near-surface turbulent flow and scalar fields. A single optical fiber can be utilized for observations across different media, like air, water, ice, snow, mineral soil, or plant tissue and therefore has an advantage to most in-situ or remote-sensing techniques (Thomas and Selker, 2021).

$$T(x,t) \; \alpha \ln(\frac{T_{AS}(x,t)}{T_S(x,t)})$$

<div align="right">(2)</div>
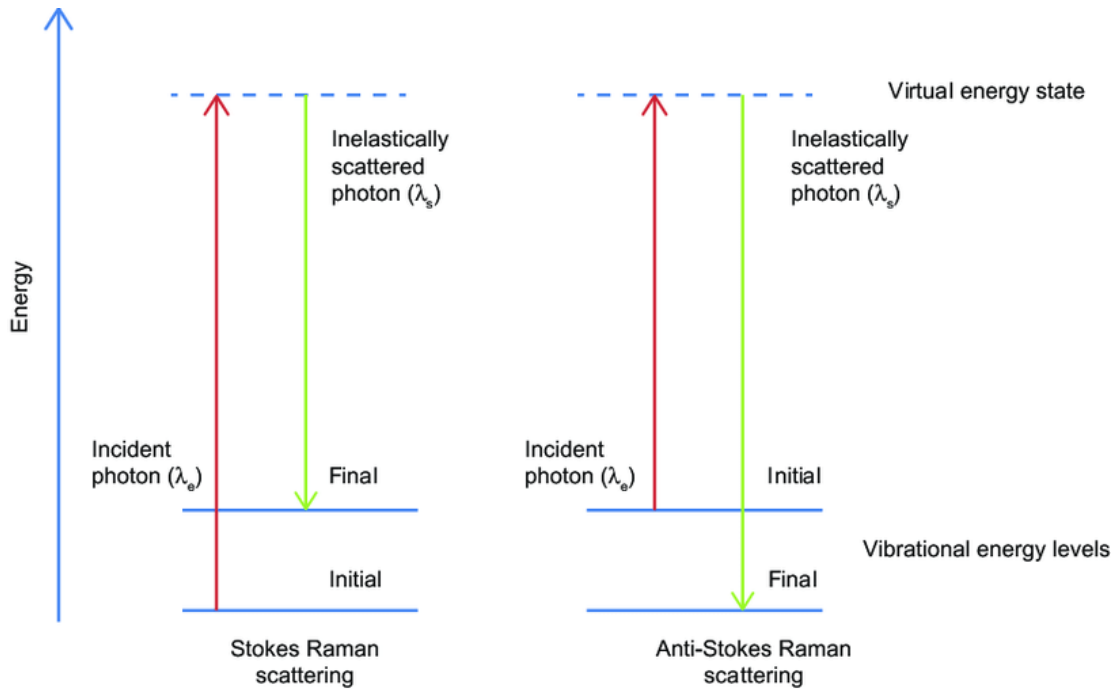
Figure 1: Temperature independent Stokes Raman scattering and energetic Anti-Stokes with temperature depending amplitude (Wang et al., 2016)

The foundation of all FODS applications relies on the DTS technique. To convert the raw measurement data into temperatures a calibration process must be performed. This involves the independent measurement and knowledge of the temperature of a particular section of the fiber-optic cable sensor, referred to as the reference section. In its traditional form, the calibration procedure is done using water volumes contained in thermal insulated containers. The reference section of the fibre-optic cable is passed through the liquid volume, which is heated or cooled on a defined temperature using aquarium heaters or crushed ice, respectively. While in theory this method offers an inexpensive, uncomplicated construction, easy-to-transport, and environmental harmless temperature reference for online or post-field calibration, in practice several disadvantages are accompanied with this method. To name only the few most important, shortcomings include non-stationary bath temperature due to insufficient insulation of the water volume through outside conditions with radiative forcing and extreme temperatures, as well as uncertain cooling or heating cycles of the electronic control circuit. One should mention, respectively systematic spatial heterogeneities, consequently with imperfect mixing at the water ice interface and at the corners of the container. For the application in subfreezing environments the use of lower freezing liquids is required. To translate the primary measured intensities of Stokes and anti-Stokes photons to the secondary desired temperature signal, *SoPhaBs* were used for cold and warm temperature calibration, eliminating the need for antifreeze liquids at the artic super site (Thomas et al., 2022).

2.1. Site description

The AGF350-850 field class took place between January 27.02 and 20.02.2022, in the vicinity of the town of Longyearbyen, which is situated at 78.218 lat and 15.638 lon. Longyearbyen is the northernmost year-round inhabited town in the world, with a population of around 2.350 people. It is located on the main island of Svalbard, which is part of Norway. Svalbard is located around 1.000 km north of the Norwegian mainland, with its coastline bordering the Barents Sea and the Greenland Sea.

6

Figure 2: Orographic scheme of Adventdalen valley (Copyright Norwegian Polar Institute). The orange marker shows the location of the observation site at the aurora station. Adventdalen is surrounded by mountains and glacier areas. Several side valleys, Endalen, Todalen and Mäiardalen, lead into the main valley. On the northwest side it borders with the Adventfjorden.

The main place of investigation during the project lies in the valley Adventdalen, which borders at Longyearbyen on its westside. Adventdalen is about 30 km long and got extended by the Adventfjorden. The fjord is the connection of Longyearbyen to Isfjorden and to open waters. The environment is glacially overprinted and confined by mountains (Bassen, 960 m a.s.l.) in the north and multiple plateaus in the south. Several side valleys lead into Adventdalen causing katabatic airflows into the plain (see Figure 2). The local wind field is determined by the orography. Two main wind directions result from the orographic setting. Both dominant wind directions occur alongside the fjord axis, because of the channelling effect between the coastline and the topography. Northwest landward winds appear mainly within the range from 1.6 to 10.8 ms^{-1}, while the southeast seaward winds are weaker and mostly in category between 0.0 to 5.5 ms^{-1} (Figure 3).
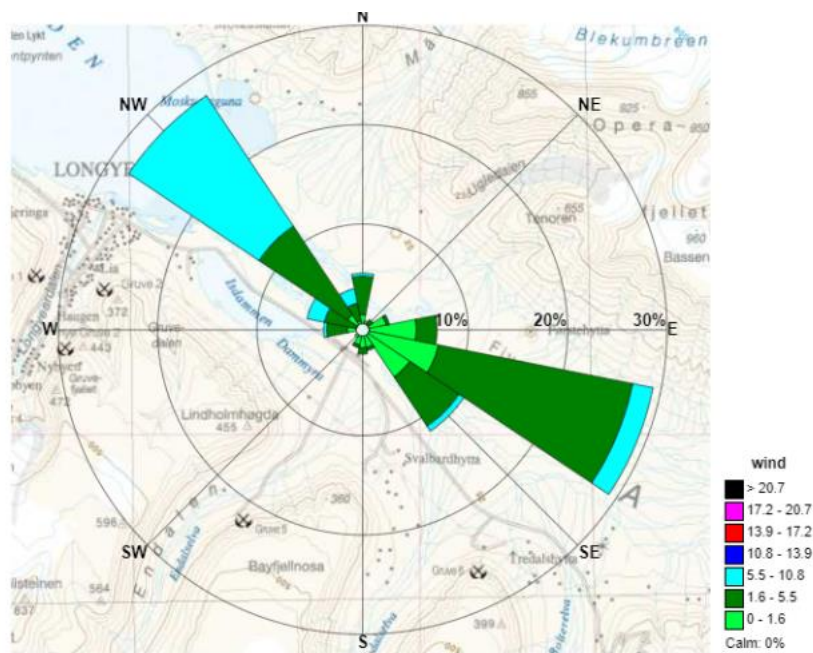
Figure 3: Wind rose of the Adventdalen valley (Copyright University centre in Svalbard). Device: Young 05103, 08.05.2021-08.05.2022. The period was chosen as full-year extension of the field campaign of this thesis. Two main wind direction predominate the flow pattern statistical within this year, both along the fjord axis, northwest wind from the seaside near Longyearbyen and slightly weaker wind from southeast direction out of the valley. In comparison the extract of the observation 10.02. - 17.02.2022 is only characterized by the SE-wind (Figure 26).

7

The temperatures during the observation time lay between min. -23.98 °C and -4.3 °C as maximum (Figure 4). Despite the high northern latitude, the climate in Longyearbyen is strongly influenced by the ocean and it is characterized by relatively mild temperatures due to the effect of the West Spitsbergen Current, which brings warm and salty water while running poleward (Haugan, 1999). The FODS measurement, which started at the 10.02.2022 and ended on the 17.02.2022 (blue box, see Figure 4), was characterized by the ending of the polar night and strongly by daily increasing twilight time. On the 19.02.2022 of February the first direct sunlight reached the summit of Bassen. The setup was never lit by direct sunlight.
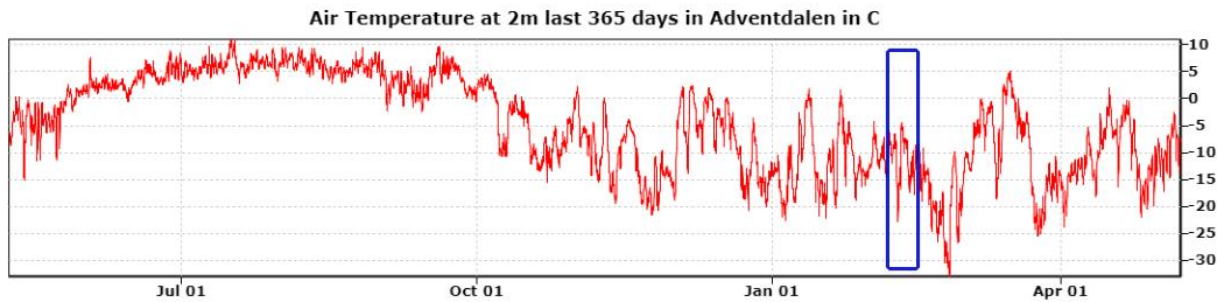
Figure 4: Air temperature measured in Adventdalen; PT100 2m and 10m, 08.05.2021-05.08.2022, (Copyright University centre in Svalbard). The section of the observation period is marked in the blue box (10.02. - 17.02.2022).

2.2. Setup

As place for our observation the old aurora station of UNIS was chosen. The station was also used as base camp during the field work time and provides a stable power supply for all devices. The aurora station is located 4.5 km to the southeast of Longyearbyen. The elevation of the area measures 6 m above sea level. The measurement DTS device (model XT, Silixa, Borehamwood, UK) was set up in the building, as well as the two FO calibration devices *SoPhaBs*, for moderate and more uniform temperatures for the calibration. Our performed setup consists of two horizontal sections of high-resolution optical fibre leading from the station over 125 m distance to the meteorological tower (Figure 5). At the 10 m meteorological tower two columns made from reinforcement fibre with a height of 2.5 m a.g.l. (PVC) and 1.5 m a.g.l. (bare fibre) were assembled with the FO fibre coiled around (see 1.1). In case of the PVC covered fibre the array leads towards and backwards the tower, while the bare fibre could only be set up in one direction due to technical issues.

In proximity to the two FODS columns an USA was mounted at the frame of the meteorological tower (Figure 6). A CR6 datalogger from Campbell Scientific collected data from four PT100, which were attached to the FO columns, respectively placed in the snow to record temperature data for calibration/verification reasons. The measurement device from Silixa captures its data along the fiber axis, which is referred in the unit LAF (m). The array circumference a total length of $l_{PVC} = 620\ m$ respectively $l_{bare} = 315\ m$, which results due to the capabilities of the Silixa in an along fiber resolution of $\Delta LAF = 0.254\ m$ (Table 1). As temporal resolution $\Delta t = 10\ s$ were chosen at the Silixa XT. Each array was installed with a different type of optical fibre. The first was equipped with $d_{PVC} = 900\ \mu m$ white jacket PVC, tightly buffered (AFL, Duncan, SC, USA) and the second FO cable type with $d_{bare} = 250\ \mu m$, clear coating on the outside, termed *bare* fibre (see Figure 7). Both types come with the same 50 μm light transmitting core.

Radiation data at the FODS sampling site was provided by UNIS. Global radiation and reflected radiation were measured by two CN3 pyranometer and the longwave radiation terms were recorded by the pyrgeometer CG3 (Kipp & Zonen B.V., Delft, ZH, the Netherlands).
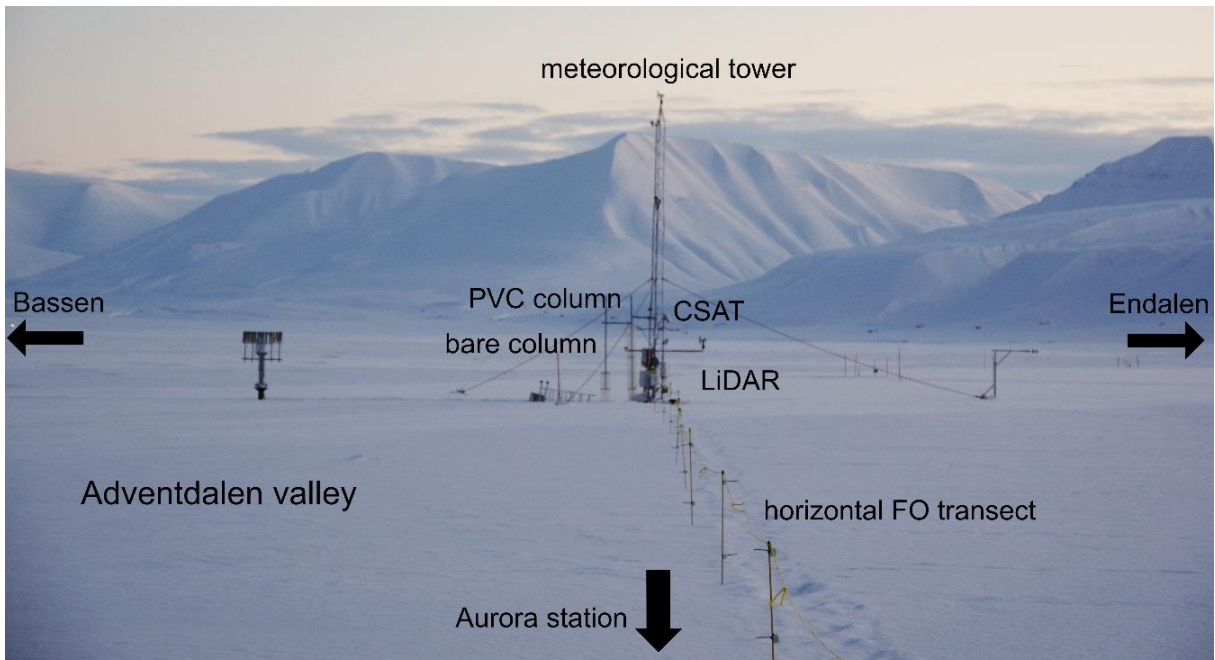
Figure 5: Photography of the observation site (Christoph Thomas) and schematic of the FODS sections. The 10m tower was used as stable structure for the attachments to the FO columns. For an undisturbed snow cover all passenger traffic was transacted via the separate walkway. The USA and the snow LiDAR were mounted next to the FO columns. The Endalen side valley is located to the right side of the picture and the mountain Bassen to the left in north-east direction.
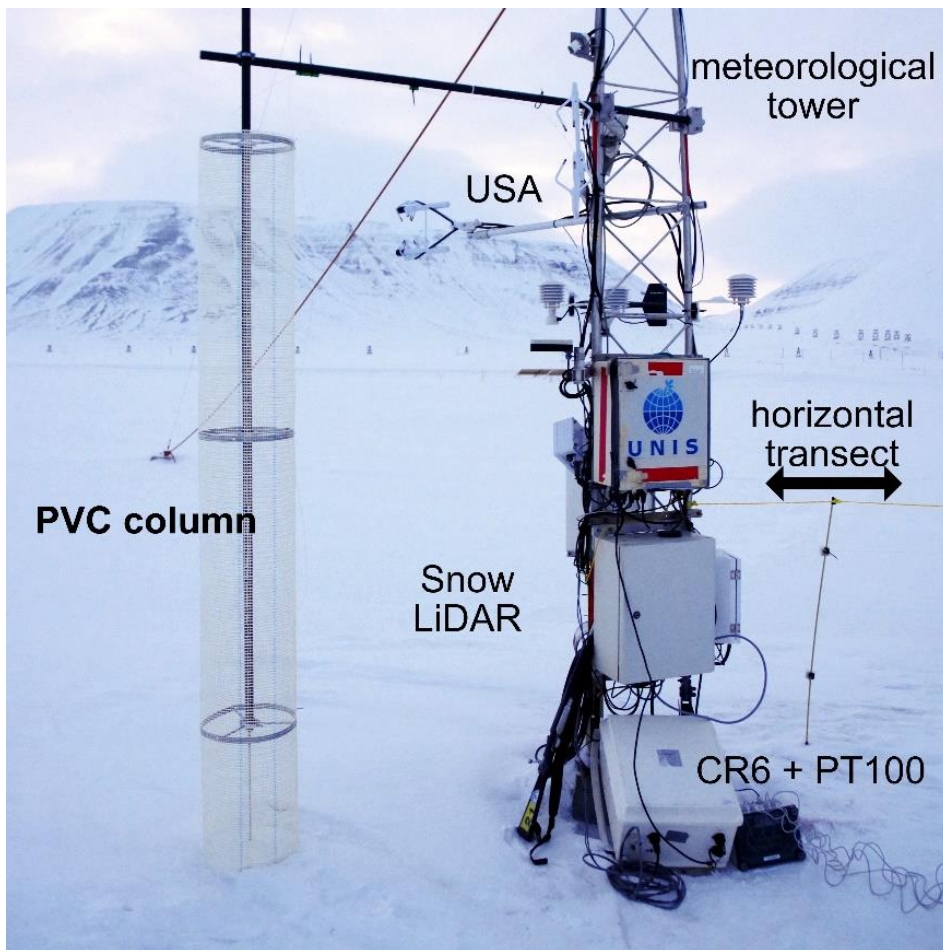
Figure 6: Installed PVC FO column in Adventdalen next to the meteorological tower equipped with the USA and CR6 datalogger. The FO column was placed at ground level measuring the snow layer inside and the air temperature above the interface. Carbon fiber tubes and an aluminium spike obtain a secured position at the upper and lower end.

In our experiment the ΔLAF was limited to 0.254 m due to the instrument-specifications. By helically coiling the fiber optic cable around a column made of reinforcing fabric (Maxit Baustoffwerke GmbH, Krölpa, TH, Germany) the vertical resolution was increased to the millimetre scale. The support structure was made of white reinforcing material with a mesh size of 0.01 m. This material is made of glass fibres and helps to reduce radiation errors for the following reasons: The white fabric strands and fiber cables were assumed to have an equal diameter and albedo, resulting in negligible radiative heating or cooling (Sigmund et al., 2017). Moreover, they exhibited similar emissivity, which further minimized the effect. The high air permeability of the meshed fabric was expected to allow strong convective heat exchange between the fiber-optic cable and the air, reducing the temperature differences between fabric, fiber, and the air. For a minimum contact surface, both fibres were guided between the grid zone of the reinforcement fiber and attached with UV-hardening glue at the position (Figure 7). Both columns had a circumference of approximately 1.00 m, which was equal to four times the LAF resolution of the DTS instrument. To achieve the highest vertical resolution of air temperature and its gradients close to the surface ground, the individual fiber coils were spaced at 1 cm vertical separation distance in the lowest 1 m part of the columns and at 2 cm respectively 0.04 m in the upper 1.5 m/ 2.5 m sections (Table 1). As a result, the FO system enables a maximum resolution of 0.0025 m in the lowest section of the column.

Table 1: Specification of the FODS column and properties of the used FO fiber types

FO cable type	PVC	bare
Resolution ΔLAF (m)	0.254	0.254
Resolution Δz (m)	0.00254	0.00254
Resolution Δt (s)	10	10
Ø Diameter fiber (μm)	900	250
Time of FODS measurement		
Start	10.02.2022 08.30	14.02.2022 20.00
End	17.02.2022 13.00	17.02.2022 13.00
helical rise (m/FO turn)		
until 1 m	0.01	0.01
1m to 1.5m	0.02	-
1.5m to 2.5m	0.04	-

Compared to the NYTEFOX experiment the columns were designed with stainless steel support rings and a thin aluminium guidance to the ground (see Figure 6) to increase the quantity of artifact free segment, especially at the snow-air surface (Zeller et al., 2021). The position of the aluminium guidance was predrilled into the permafrost. The upper position was secured by the carbon fiber tubes attached to the main tower (see Figure 6). Within the installation the snow cover around the columns was not affected. To ensure a natural untouched snow cover without local compaction at the place where the FO column was installed, the snow was removed at first at the shape of the reinforcement fiber and remaining gap closed itself through snow drift and precipitation within the next day.
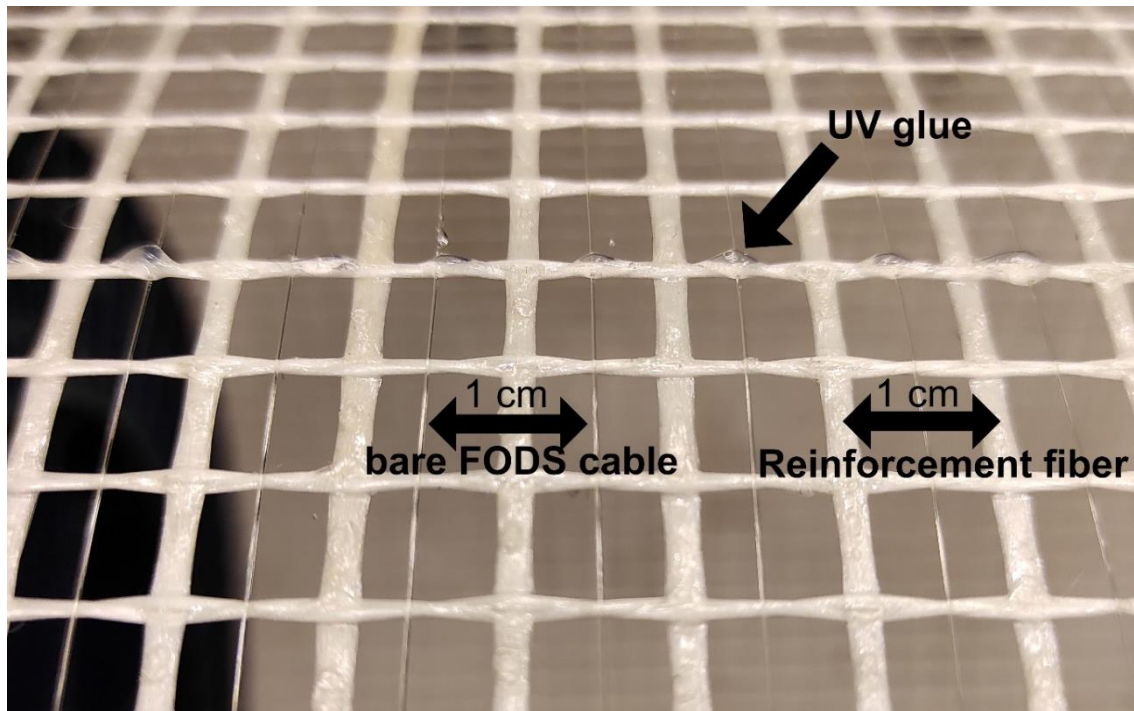
Figure 7: Photography from the mesh structure of the reinforcement fiber. The bare fiber was winded between the space between the grid and glued with UV clue to reduce the contact surface. Both materials resemble in its emissivity. The setup was designed to minimize the conduction error and to enable maximal permeability.

2.3. Data processing

The calibration of the FODS data was done with *pyfocs*, an open-source library developed by the Micrometeorology Group of the University of Bayreuth (Freundorfer et al., 2021). The basis for FODS data processing are the recorded Raman backscatter intensities, which are measured by the DTS instrument. In the first processing step the incoming raw signal, with the intensities at the Stokes and the Anti-stokes, needs to be assigned to the predefined temperature environment inside the *SoPhaBs*, to get a meaningful connection of the temperature environment around the fiber.

Since the measurement device only collects information about temperature in one dimension, i.e., length alongside the axis of the fiber, the length sections need to be referred to the actual geographically three-dimensional coordinates of the FODS array in the second step. Therefore, the array was mapped by establishing a reference between an induced temperature peak on the FO cable with the geographical position, measured by a GPS device. This procedure was executed at the beginning and ending of the two horizontal arrays, at both FO columns, as well as at each transition of the helical rise of the coiled fiber. Thus, each point of interest could be filtered out, providing an artifact free dataset with known locations to work with.

The processing of the USA data was carried out post-field and was not implemented as part of this thesis. The eddy covariance was calculated with the *bmmflux* tool provided from the micrometeorology department (Thomas et al., 2009).

2.4. Analysis

The output of the files after calibration with *pyfocs* was provided in the *netcdf* format. The programming for the entire analysis, including the processing was performed with the language Python 3.10 (van Rossum, 2015). The open-source software *Spyder* was used as programming interface, offering integrated development environment for scientific programming.

2.4.1.   Radiation and energy balance model

To quantify the radiation errors in the coiled DTS system, a modelling approach was used to estimate the divergence of FODS temperature. An energy balance was employed to create a model, which also considered the heat conduction to/from the support structure, contributing to the overall error (Sigmund et al., 2017). This model can be used under various meteorological conditions or with different material properties, providing a versatile tool for assessing the performance of the coiled DTS system. The investigation by Sigmund et al., 2017 was used as guidance for this modelling approach. The calculations, that were made, are based on this previous research. Subsequently the model was adapted to match the conditions of the polar night.

A FO cable is used in the DTS method as sensing element. As other sensors too, the fiber is exposed to its environment and therefore subject to the surrounding airflow and radiation regime. To quantify the significance of the error through radiative forcing, an energy balance was modelled by Sigmund et al., 2017 around the boundaries of the coiled DTS system. The model includes the ned radiation balance, with the longwave radiation terms, the heat transfer through forced convection and the conduction term at the contact surface with the support structure.
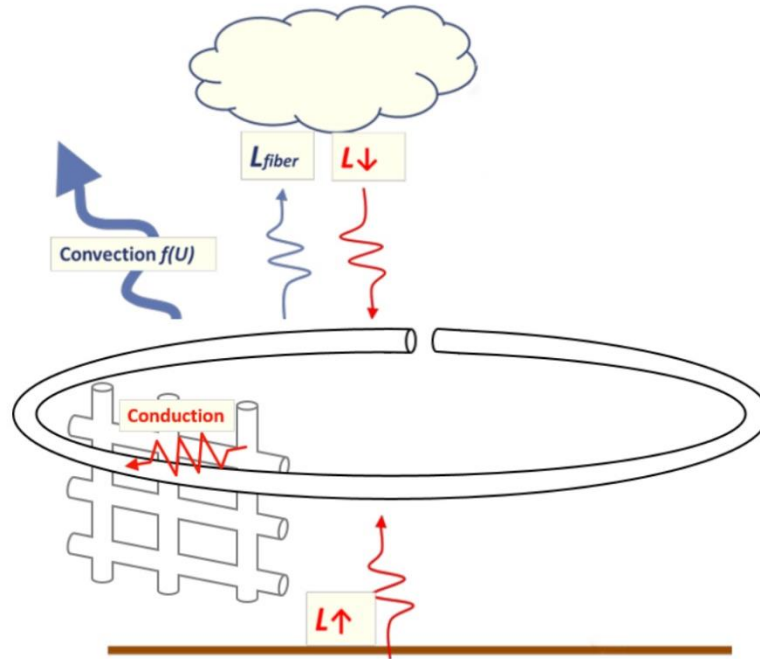
Figure 8: Composition of error factors on one FO turn adapted for the application in the polar night, separated into outgoing terms (blue) and incoming terms (red). The longwave radiation is differentiated into emitted radiation according to Stefan Boltzmann Law and incoming radiation share from surface radiation and atmospheric counter radiation. Energy loss through conduction with the reinforcement fiber and the convection term proportional to the windspeed. The figure was adapted from Sigmund et al., 2017.

The equation represents a term of the involved energy fluxes, to and off, one fiber winding. By integrating the flux densities ($Js^{-1}m^{-2}$) over the cylindric surface area of the FO winding, all terms get the unit Watt (Js^{-1}):

$$Q = Q_{in}^{cond} + Q_{in}^{S} + Q_{in}^{L} - Q_{out}^{L} - Q_{conv}$$

$$(3)$$

One can express the total specific energy flux Q to and from a fiber-optic coil as a sum, where Q_{in}^{cond} represents the incoming energy flux from conduction between the fiber cable and reinforcing fabric, Q_{in}^{L} represents the incoming energy fluxes longwave radiation respectively, Q_{out}^{L} denotes the emitted

longwave radiation from the fiber, and Q_{conv} represents the energy exchange due to turbulent convection with the moving air in the outward direction. The energy fluxes directed towards the fiber-optic cable are considered positive as incoming fluxes, whereas the energy fluxes directed away from the cable are considered positive as outgoing fluxes. The shortwave radiation term Q_{in}^{S} was neglected since this research question wants to investigate on the application of different types of fibre during polar night, means under the absence of solar radiation.

$$Q = c_p \, \rho \, V \, \frac{dT_s}{dt}$$

$$(4)$$

According to the law of conservation of energy the sum Q of all outgoing and incoming fluxes equals the rate of change of internal energy stored in on FO winding. Q can be expressed with the heat capacity c_p (J kg^{-1} K^{-1}), the density of the FO cable (kg m^3), the volume (m^3) and T_s the fibres surface temperature (K) and the time (s) (Eq. (4)).

The convective heat transfer coefficient h is primarily determined by the speed of the wind and can be characterized mathematically as:

$$h = C \, (2r)^{m-1} \, Pr^n \, (\frac{Pr}{Pr_s})^{\frac{1}{4}} \, K_A \, \vartheta_A^{-m} \, U_N^m$$

$$(5)$$

To determine the convective heat transfer coefficient (Eq. (5)), several parameters must be taken into consideration. These include the radius of the fiber cable r (m), the thermal conductivity of air K_A (J s^{-1} m^{-1} K^{-1}), and the kinematic viscosity of air υ_A (m^2 s^{-1}) (Sigmund et al., 2017). The dimensionless parameters C and m are also important and were assigned values of 0.52 and 0.5, respectively, for Reynolds numbers ranging from 40 to 1000, and values of 0.75 and 0.4, respectively, for Reynolds numbers less than 40 (Hartnett and Irvine, 1987). Pr and Pr_s (1) represent the Prandtl numbers at air and fiber temperatures, respectively, and were calculated by linear interpolation and extrapolation (Bejan, 2013). The term (Pr Pr_s^{-1})$^{1/4}$ was assumed to be 1 since it remains close to this value even for fiber and air temperatures as low as -20 and 0 °C, respectively. Finally, the dimensionless parameter n was set to 0.37, since all Pr values were less than 10 (Hartnett and Irvine, 1987). It should also be noted that for straight fiber cables, only the wind velocity component U_N (ms^{-1}) that is normal to the fiber contributes to convection, whereas for coiled FO cable, the total three-dimensional wind velocity can be used due to its different geometry. U_N in dependency to the surface distance was calculated by the function of the logarithmic wind profile.

The emissivity ε (-) for both FO cables is unknown. Therefore, ε_S was determined by solving the Stefan Boltzmann law. For this purpose, the energy balance was simplified by assuming the latent heat Q_s flux to be neglectable during the polar night, see also Equation (6). The gained dataset was filtered for windspeed higher than 4 ms^{-1}. For high overflow velocities of the FO winding the effectivity of the heat transfer by convection becomes a multiple of the conduction and thus it can be justified to neglect the conduction error (Baehr and Stephan, 2019). The sensible heat flux Q_H was taken from the data of the USA. $I_\downarrow$ and $I_\uparrow$ (J s^{-1} m^{-2}) represent the average values of the fluxes of longwave radiation directed downward and upward, respectively, per unit surface area of the fiber-optic winding. The constant σ_S (J s^{-1} m^{-2} K^{-4}) is known as the Stefan–Boltzmann constant. P indicates the power (Js^{-1}) and A represents the surface (m^2).

$$P/A = I_\uparrow = Q_H - I_\downarrow$$

$$(6)$$

$$\varepsilon = PA^{-1}\sigma_S^{-1}\,T_f^{-4}$$

$$(7)$$

Combining Equation (3) to (7), one obtains a correction model, which provides a corrected fiber temperature T_{Af}, which estimates the influence of the error components during polar night (Eq. (8)). Since earlier research with this model has shown, that conduction term, is considerable small, it was not taken into account (Sigmund et al., 2017).

$$T_{Af} = T_f + \frac{1}{h}\left(\frac{1}{2}c_p\rho r\frac{dT_s}{dt} - \frac{1}{2}(L_\downarrow + L_\uparrow)\varepsilon + \varepsilon\sigma T_f^4\right)$$

$$(8)$$

2.4.2. Snow height detection

To calculate the heat diffusivity inside the snow layer by use of the FODS measurements, one needs to know the distribution of snow around the column. In relation to the hypothesis 2 and the correlation of turbulence with the heat diffusivity inside the snow mass, it is necessary to calculate on a defined height below the snow, because otherwise the fluctuations in the distribution may be reflected in the signal and reduce its meaningfulness. At the sensing site, the depth of the snow layer is subject to fluctuations through direct snow fall, drift, and sublimation. But also, turbulence induced snow drifts, causing accumulation or loss of snow mass. Due to the physical form of the FO column, point based determination of the snow height provides an inadequate expression of the reality, since the snow tends to accumulate around the column of reinforcement fibre. Within the analysis different approaches were done to obtain the snow depth at the site location:

During one method the high vertical resolution of the FO column was used to calculate the standard deviation of the temperature σ_T (K) over 15 minutes periods. σ is defined as the square root of the variance.

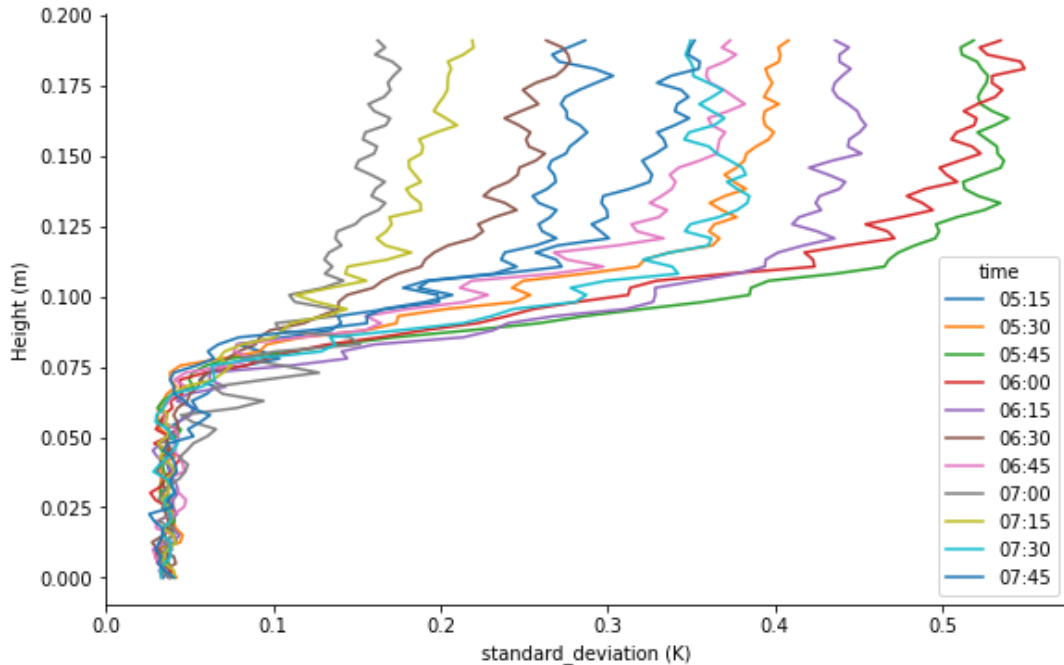*Figure 9: Development of the standard deviation of the temperature within 15 minutes block-averages. Inside the snow layer the variance stays constant within the averaging period, while within the stable boundary layer σ_T is varies and increases strongly. Depending on the conditions of the atmosphere the standard deviation respectively the variance stabilizes on different levels. The sample dates from the 12.02.2022.*

On a single profile along the height, the standard deviation inside the snow layer tends to stay on an explicitly low level. Inside the surface boundary layer σ_T increases strongly while the trend passes its turning point. In the overlying atmosphere σ_T stabilizes again depending on the turbulent regime on different level, as shown in Figure 9. Regarding the further goal, a threshold was chosen at the point when σ_T changes from linear trend, at 0.08 K. According to the Figure 10 the threshold of σ_T=0.08 K is indicated by the yellow area of the colourmap. Based on the height index of this threshold the snow height was determined. Several conditions were implemented to obtain a meaningful trend of the snow height. Figure 10 indicates the height of the threshold. However, the trend of threshold condition shows some deflection, which are not significant for the variability of the snow height. This includes the zero index, which was ignored by the calculation, respectively the time stamps, in which the height index of σ_T=0.08 K exceeds the 0.2 m mark, were set on a minimum snow level of 0.04 m. The last condition was added, to avoid any case in which the snow height is overestimated, since the numeric approach is dependent to be inside the snow medium and any divergence produces erroneous values for the heat diffusivity.

Subsequently the signal was decomposed with the Bior5.5 wavelet library (see also 2.4.4) to eliminate the high fluctuations, but to be more realistic for actual trends of the snow height (Thomas and Foken, 2005). The low-pass data, respectively the snow depth trend, from the biorthogonal filter was used as a template for the subsequent analysis of the heat transfer (see Figure 12). Furthermore, the determined course was compared to the data of the snow lidar at the turbulence tower in Adventdalen. The data was provided by the Norwegian Centre for climate services. It must be noted that the place of recording was shifted in 2 m distance to the FO array, so the actual height cannot be compared, but the variation caused by snowfall can be seen. Snow depth estimate results from the FODS measurements are presented in Figure 11, each 15-min-average from the standard deviation is represented by a blue cross, the low-pass signal from the Bior5.5 is indicated in the red line and the LiDAR data is shown in yellow colour.

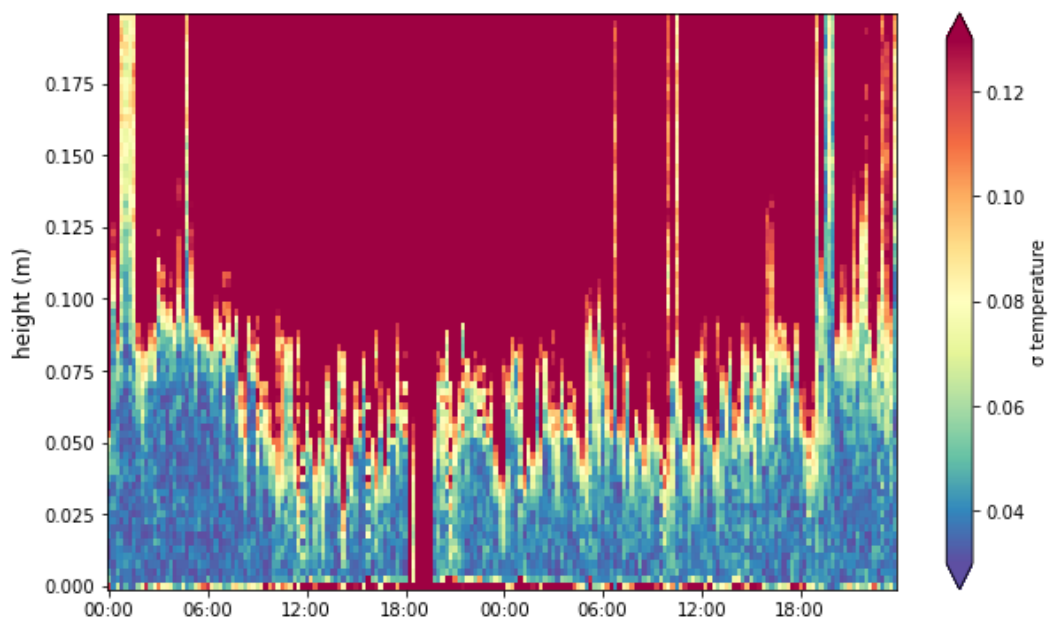*Figure 10: Exemplary two-day period for the determination of the snow height with the standard deviation of the temperature. The threshold of $\sigma_T = 0.08$ K is shown in yellow colour. The data was aggregated to 15min packages. In the afterward procedure the unphysical "snow heights", overshooting standard deviations and zero levels, were removed from the profile. For detailed information, see 2.4.2.*
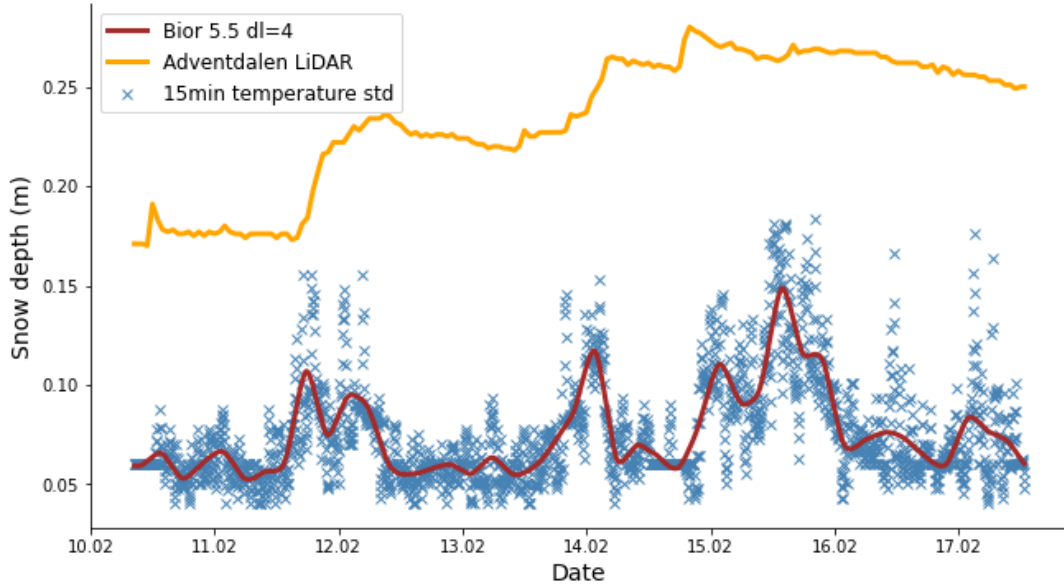
Figure 11: Obtained trend of the snow depth in Adventdalen compared against the snow LiDAR data from the Norwegian Centre for climate services (https://seklima.met.no/). Each blue mark represents the first height, which exceeds the threshold of 0.08K of the temperature's standard deviation. The red line plot indicates the wavelet decomposition level 4 with Bior5.5 of the temperature's standard deviation. The LiDAR data as reference from the sensing site was collected at a 3-meter distance to the FO column.

2.4.3. Thermal diffusivity

Investigation on the thermal diffusivity of snow is a challenging task that requires careful consideration of the limitations and accuracy of different measurement techniques. The thermal diffusivity refers to the ability of a material to conduct thermal energy relative to its ability to store thermal energy, i.e., it describes how fast temperature spreads through a material, and it depends on two fundamental physical properties: thermal conductivity and heat capacity. α can be resolved as the quotient of the heat conductivity λ (J s^{-1} m^{-1} K^{-1}) and the density ρ (kg m^{-3}) times the heat capacity (J kg^{-1} K^{-1}), see Equation (10). However, measuring these properties directly is challenging and inaccurate. Firstly, snow metamorphism refers to the changes that snow undergoes over time due to forcings through temperature, precipitation, wind, and solar radiation. Moreover, the process of measuring these properties can cause compaction, which further affects their accuracy. Secondly, traditional methods for determining thermal conductivity and density are generally limited by their temporal resolution. These methods typically involve taking measurements at discrete time intervals, which may not capture the dynamic changes that occur in snow properties over time (Oldroyd et al., 2013).

$$\frac{d\mathrm{T}}{dt} = \alpha * \frac{d^2\mathrm{T}}{d^2z}$$

(9)

$$\alpha = \frac{\lambda}{\rho c}$$

(10)

According to the Equation (9) the one-dimensional heat equation in direction of z is given as the temporal change of the temperature (K) on each point of the heat conducting object proportional to the heat diffusivity. The differential equation links the stationarity of the temperature with the second derivative in space. Which in our case is the same as the curvature of the temperature with height (Baehr and Stephan, 2019).

To quantify the heat transport within the snow layer, this research question focuses on the determination of the heat diffusivity inside the snow, by using finite differencing as a numerical

16

method to solve the heat equation in time and space for a range of diffusivities. The process involved iterations to reduce the possible range of thermal diffusivities, with the goal of minimizing the root mean square error between the temperatures that were measured and those that were predicted. In theory, the size of the simulated domain should be minimized because this method calculates a *bulk* thermal diffusivity value that applies to the entire area being simulated. On the other hand, including a greater number of temperature measurements in the simulated area can improve the accuracy of the physical description, particularly in regions with significant gradients or curvature. Additionally, it offers more data points to compare the root mean square errors when optimizing the thermal diffusivity value. Next to the differential equation, which describes the relationship between the variables involved in the problem, finite differencing requires further information, like boundary conditions and initial conditions. While the boundary conditions, referred to as BC, specify the behaviour of the solution at the boundaries of the domain, the initial conditions provide information about the solution at the starting time or at some other point in time. With this information, we can apply the finite difference method to approximate the solution of the differential equation at discrete points in space and time. The high resolution FODS dataset, provides the obligatory information of the temperature in time and space respectively on the z axis to numerically reduce the differential equation to several ODEs. Within this research the heat equation was solved numerically according to the Euler method, to be more precise, the implicit or backwards approach was chosen (Bärwolff, 2020). The Euler implicit or BTCS was applied, i.e., the future value of the solution at the next time step is computed by solving a linear equation that involves both the current value of the solution and the future value of the solution. This linear equation is obtained by discretizing the differential equation using a backward difference approximation in time and a central difference approximation in space. As difference quotient the central difference was used to get a minimized error and ensure a high accuracy. The accuracy is higher with the central difference quotient when inserted in a differential equation because it takes into account both forward and backward differences, leading to a cancellation of the leading error term that is present in the forward or backward difference methods alone (Bärwolff, 2020).

The determination of α is based on sliding vertical profile section (Figure 12) with a bandwidth of twelve measurement bins, equally to 0.0305 m, with a constant spatial distribution of dz=0.00254 m. In turn the spatial resolution dz derives from the capacity of the FODS column, describe in chapter 1.1, by projecting the helically aligned temperature datapoints to one imaginary straight, the z-axis. The entire FODS temperatures were recorded as averages of dt=10 s over the observation period. Exactly the FODS resolution causes the necessity for the Euler implicit method on this dataset and the disqualifying of the explicit method, that was chosen in earlier research (Oldroyd et al., 2013). BTCS stands out, not only because it is always numerically stable, but FTCS (forward in time, centred in space) scheme is subject to a condition to reach numerical stability, see also Equation (11). The explicit Euler method for the one-dimensional heat equation, as derived using von Neumann stability analysis, is numerically stable if and only if the following condition is satisfied (Mukherjea, 2002):

$$\alpha \leq \frac{dz^2}{2\,dt}$$

(11)

The stability of explicit Euler is only ensured for heat diffusivities smaller or equal the square of the spatial difference (m^2) divided through two times the Δt (s). Applied to the FODS data, α means to be smaller than 3.2×10^{-7} m^2 s^{-1}, however the value nearly equals the expected reference median alpha = 2.5×10^{-7} m^{2}s^{-1} for the heat diffusivity (Oldroyd et al., 2013). Since this thesis wants to take advantage

of the high resolution and Δt and Δz are predefined by the setup, the FODS dataset is not applicable on the FTCS scheme.

Inhomogeneities at the timestamps between new FO files were interpolated linearly. The lower and upper measured temperature within the vertical profile section was set as the Dirichlet BC to reduce the differential equation to a limited number of ODEs. The dataset was split up in single intervals of either 60 seconds or 15 minutes duration. Each bundle was used to solve the differential equation and provides a single value for the heat diffusivity. The first timestep t_0 (first timestep of each 15 min/ 60 s data interval) was taken as initial conditions for the equation. Based on the results of the snow height detection, the observed height index for the snow-air interface, was used as moving reference for the input in the differential equation. Expressed differently, the supplied data packages for the determination of α, were adapted to the changing level of the snow depth. Three different located levels were chosen, delivering the basis for the initial and boundary conditions of finite differences (Figure 12). Each profile, orientated on defined heights below the surface, contained 12 datapoints within the z-axis, which equals 0.0305 m. In the temporal domain, it was found that a time series lasting 60 s is the minimum temporal resolution required. Any duration shorter than that, causes a significant drop in the resulting α range and values for α below 10^{-10} m^2s^{-1} were calculate. This result is due to shortcomings with a too small temporal domain for the numerical approach. This contradicts to the expected confidential interval of the heat diffusivity between 8×10^{-8} m^2s^{-1} to 4×10^{-7} m^2s^{-1} by Sturm et al., 1997 or by Lange, 1985.
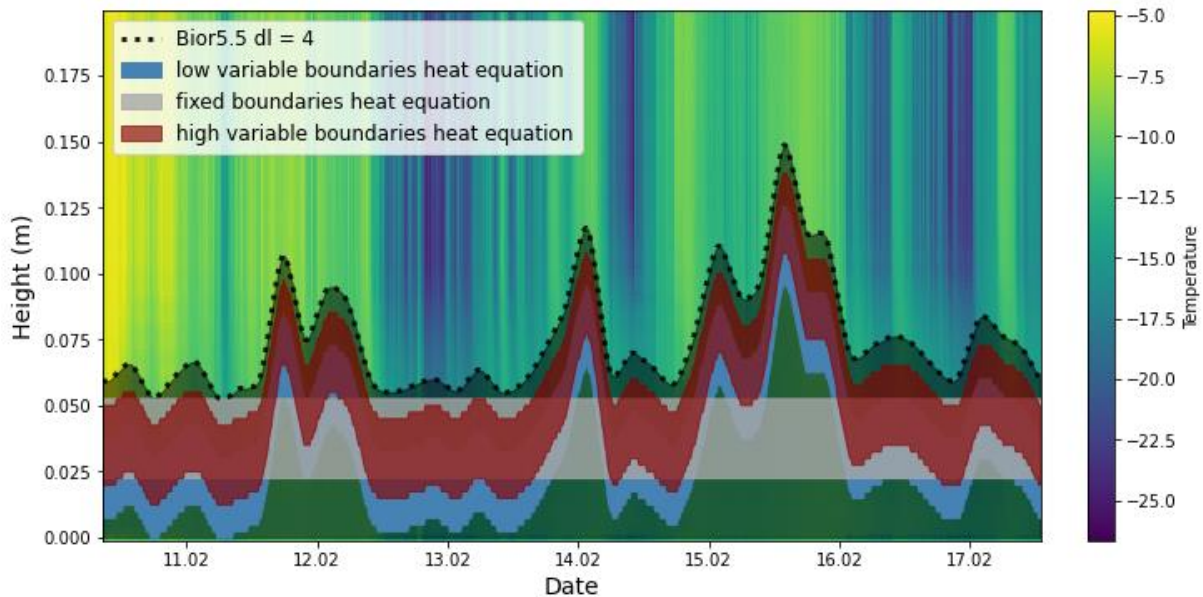
Figure 12: Presentation of FODS temperature data during the 7-day period with the computed depth of the snow volume. The snow-air interface is indicated by the dotted black line. Three moving vertical profile section with a constant spatial wide of 0.03m were added. The heat diffusivity of the snow was investigated within a fixed vertical section, shown in grey colour and variable sections indicated in brown and blue colour. Alpha was determined on running levels parallel to the surface either 0.01 m to 0.04 m (brown) or 0.02 m to 0.05 m (blue).

The RMS error is computed from the difference between the measured and predicted temperatures. To assess the robustness of the approach, the initial iteration tested a broad and imprecise range of thermal diffusivity values. This proceeding was adapted from the method used by Oldroyd et al., 2013. In this work specifically, the search involved trying out 30 logarithmically spaced values ranging between 10^{-10} and 10^{-1} $m^2\,s^{-1}$. For the second iteration, the search was refined by a linear lined up range between two points on each side of the value for the heat diffusivity with the lowest RMS from the first iteration. Subsequently, the thermal diffusivity value that most accurately represents the physical process described by the heat equation, was selected.

To further refine the model, a T-test was performed on the initial search range for the effective thermal diffusivity value at each time step, which was carried out during the first optimization iteration. This T-test was designed to ensure that the RMS error associated with the minimum was significantly different from at least three of the four adjacent points, as observed in a plot of RMS error versus thermal diffusivity. This additional step aimed at eliminating erroneous points with unreasonably low diffusivity values, by eliminating scenarios where optimization was attempted over a flat searching range and lacked a clear minimum that was statistically significant (Oldroyd et al., 2013).

2.4.4. High-frequency decomposition

The exchange of momentum, heat and mass through coherent structures were found to contribute significantly to the overall turbulent exchange between the surface and the atmosphere. One important factor in the turbulent exchange is the turbulent kinetic energy, referred to as TKE. The TKE is the energy associated with the chaotic, random motion of fluids in turbulent flow. It is a measure of the energy dissipation rate per unit mass due to turbulence expressed in units of velocity squared (m^2/s^2). In atmospheric science or oceanography, TKE is important in the study of boundary layers, where the exchange of heat, moisture, and momentum between the atmosphere and the Earth's surface occurs (Stull, 1988).

To effectively examine coherent exchange, it is vital to discover an unbiased approach for recognizing and extracting the distinct coherent incidents from the turbulent 'background' that occurs frequently. Since this research approaches to establish a connection between the trend of the heat diffusivity and the turbulent regime above the snow-air interface, a detection method was applied. Outgoing on previous acknowledgments a wavelet filter based on the biorthogonal set of wavelets BIOR5.5 was used to differentiate between the high-frequency turbulence and low-frequency coherent movements (Thomas and Foken, 2005).
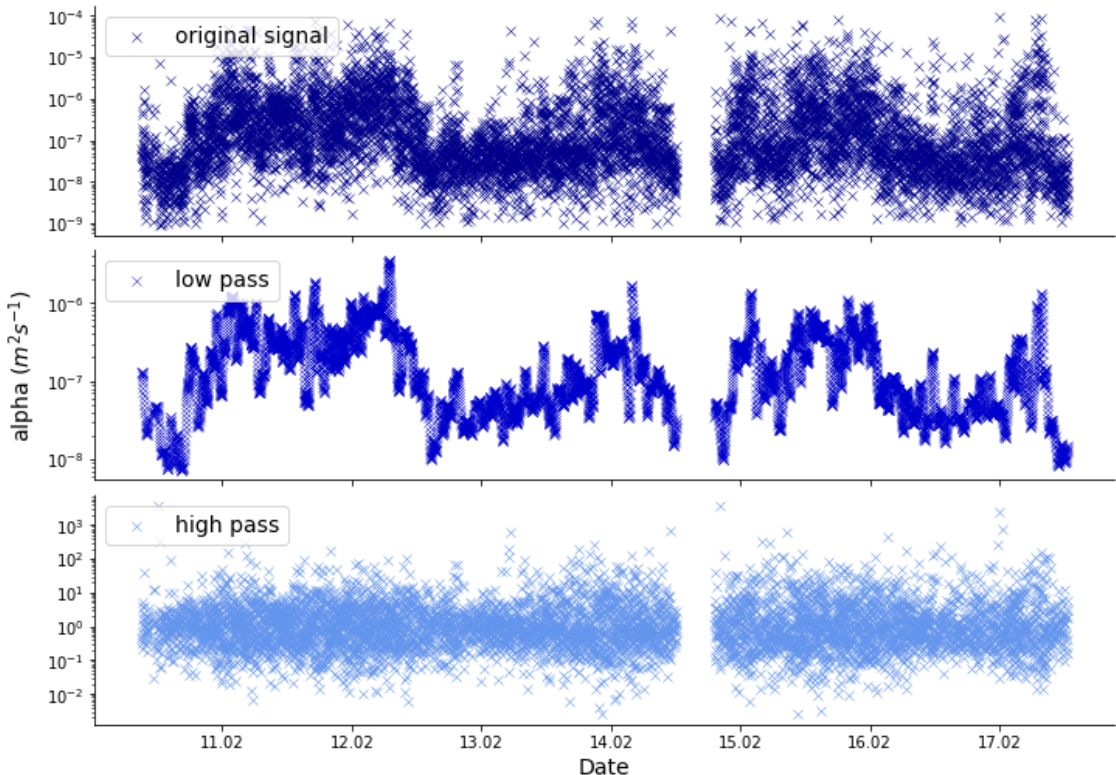

Figure 13: High and low-frequency decomposition with wavelet Bior5.5 library. Each the low pass and the high pass decomposition is shown on level=4. The high pass decomposition was denoised with the high pass data on level=1. The figure shows the data with adaptive snow height.

The methodology for the decomposition was fully adopted on this research and was applied in two different analysis steps of this thesis. Firstly, the separation of high frequency perturbations in the snow height signal to remove short-lived fluctuations, that were not associated with physical change of the snow height, without blurring the actual time of occurrence. And secondly, for the temporal differentiation of high, respectively low frequencies in the heat diffusivity signal. During the wavelet analysis of the snow height, the signal was passed through the wavelet decomposition until level four. The Bior5.5 has a peak frequency of the mother wavelet 4 Hz, resulting in a critical event duration D_c (s) according to Equation (12), i.e., all fluctuations of the signal with an event duration shorter than D are removed (Thomas and Foken, 2005).

$$D_c = \frac{a * \Delta t * \pi}{w_\psi^0}$$

(12)

From Equation (12) follows a $D_{c1} = 188\ s$ and $D_{c15} = 47\ min$ for the decomposition on level 4, with a Δt=60 s, respectively Δt=15 min. The application of the biorthogonal wavelet library enables the temporal decomposition into frequency spectra without distorting the temporal appearance (Figure 13). The low frequencies are indicated in the subplot in the centre, while the background noise with high-frequency turbulence separated from the original signal is shown in the bottom plot.

3. Results and discussion

Beginning with a short description of the general climate elements during the campaign, the section continues with the presentation of the results and the discussion of the two main research questions and hypothesis as defined in the introduction.

3.1. General characteristics

3.1.1. Air temperature and wind velocity

The measuring period was characterized by relatively mild temperatures with a mean temperature of -11.3 °C, approximately 3.4 degrees warmer than the average of the years 1991 until 2021 for the month of February (en.climate-data.org). The maximum temperature measured by the USA was -4.1 °C in 2.4 m a.g.l. and -22.8 °C the lowest measured temperature. The wind velocities ranged up to 8.6 ms^{-1} and had an average wind speed of 2.2 ms^{-1}. The wind distribution was dominated exclusively by the southeast direction along the Adventdalen valley (Figure 26).
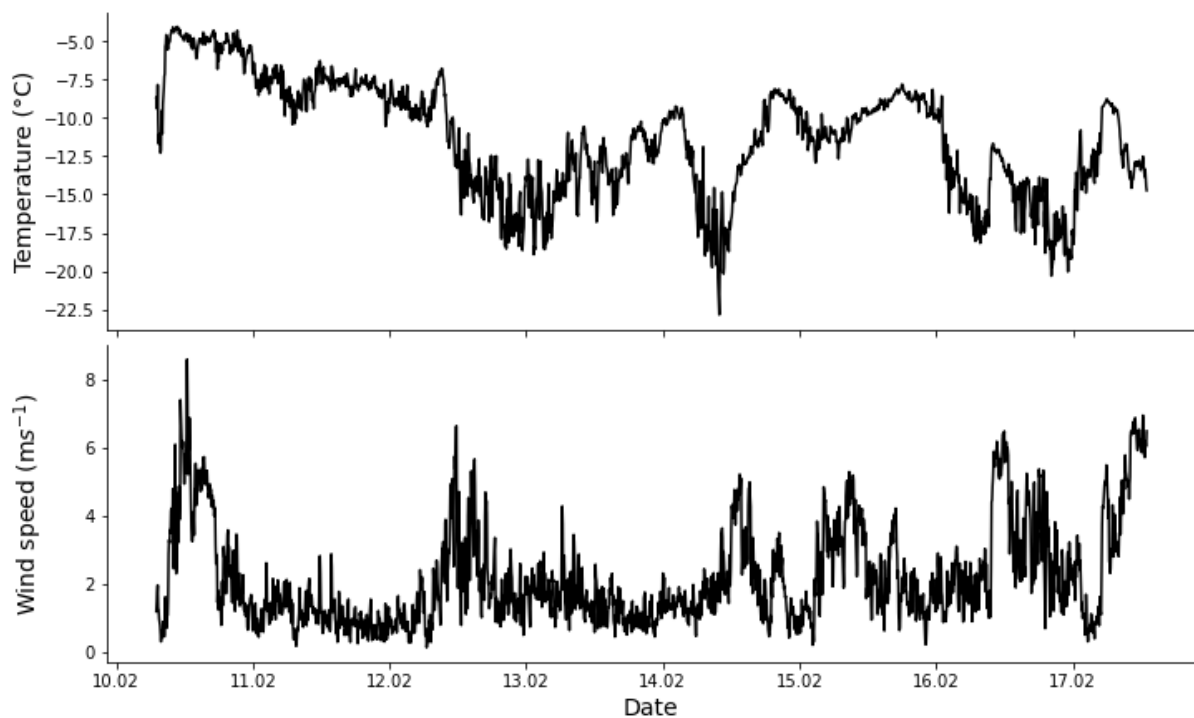

Figure 14: a) Sonic air temperature at 2.4 m a.g.l. and b) wind speed at 2.4 m a.g.l. recorded at the supersite with an USA. Measuring period: 10.02. - 17.02.2022, averaging interval of 5 min.

3.1.2. Radiation balance

The measurement period was located at the end of the polar night on Svalbard. Beginning from the 15.02.2022 the data indicates the first peak of incoming shortwave radiation around noon. Until the end of the measurement period $K_\downarrow$ reaches a maximum of 6.1 Wm^{-2}. The longwave radiation terms, exceeds the shortwave components by far and thus dominate the radiation balance Q_s. The 7-day period in Adventdalen is marked by a high cloud cover. The net longwave balance computed from amount of the longwave radiation is 1.3 Wm^{-2} in the mean and 66 Wm^{-2} at the maximum on the last day of the data recording. From the 15.02.22 to the end of 16.02.22 the sum of the longwave irradiation balance was negative, which indicates an energy gain of 26.9 Wm^{-2} at the surface. For the cumulative sum of the radiative balance see Figure 27 in the additional figures.
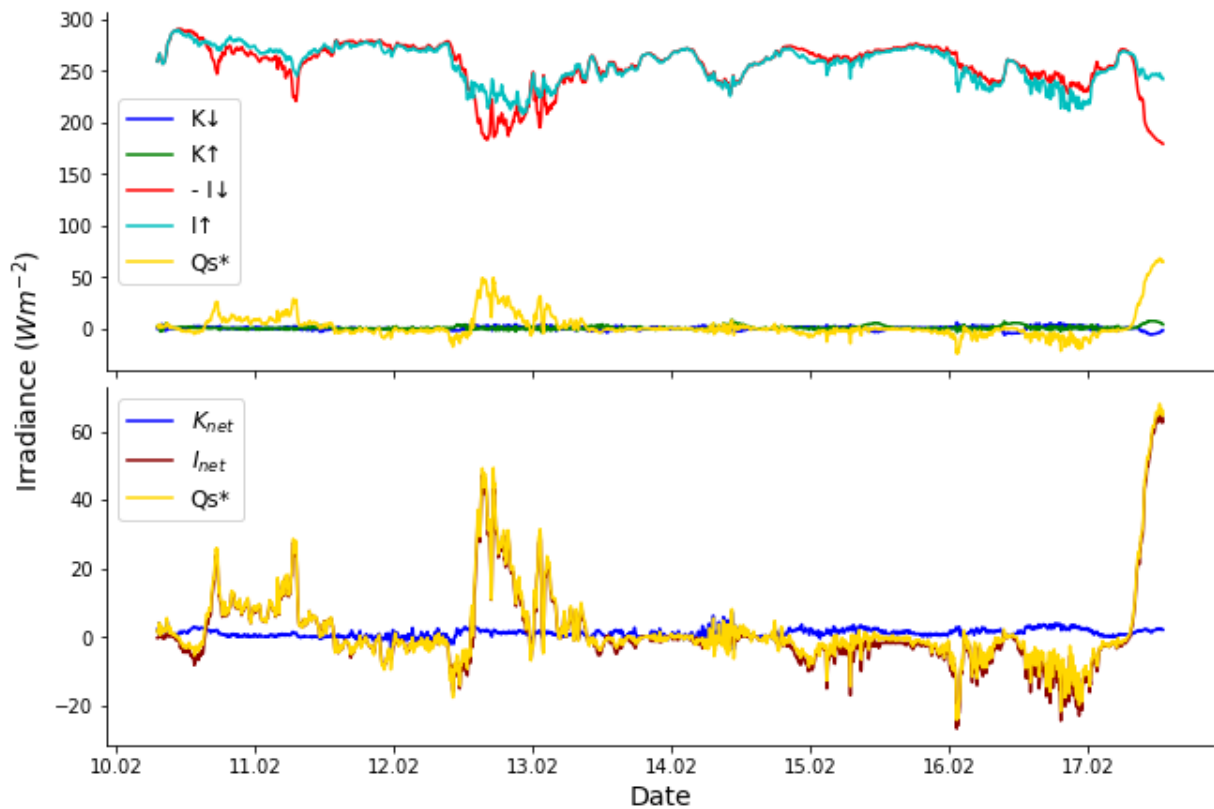
Figure 15: Radiation and energy balance recorded over the measurement period. In accordance with the meteorological sign convention, the incoming irradiance fluxes are accounted with negative sign and outgoing fluxes with positive sign. The longwave counter radiation $I_\downarrow$ was multiplied with -1 to have a better comparison to the outgoing radiation. The two shortwave components $K_\downarrow$ and $K_\uparrow$ are close to zero. Therefore, the radiation balance is determined by the longwave terms $I_\downarrow$ and $I_\uparrow$. Measuring period: 10.02. to 17.02.2022, averaging interval of 5 min.

3.2. Radiation error (RQ1)

With a pre-set sampling time of ten seconds, the time constant of the fibre is exceeded by nearly the factor 10. The conductive time scale is a function of the fibre geometry and its material properties. τ_{cond} (s) is defined as the radius of the fibre squared divided by the heat diffusivity of the optic cable. Prior research calculated a value of 1.1 s for the time constant τ_{cond} at the diameter of 900µm PVC insulation (Thomas et al., 2012). Because of the way larger sampling time, the presumption is close, that measured difference between the two fibre types are not caused by the time constant itself and instead caused by a systematic radiation error due to the variating diameter. The surface area of the PVC differs by the factor 3.6 against the thinner bare fibre resulting in a constant offset of the net radiation balance due to longwave radiation.

Quantitative analysis of the error of a sensor requires certain information about its physical environment and the underlying processes. The comprehensive energy balance model calculates the total temperature difference between air temperature and measured FODS temperature. Within the prior analysis the maximum inducing error conditions were determined. Relatively large errors would be expected due to moderate wind speed, decreasing the energy transfer, in combination with high absolute value of the longwave radiation balance, either caused by low cloud covering resulting in reduced atmospheric counter radiation or high cloud cover with warmer air mass in upper altitude.

Based on the observed radiation and wind speed data, presented in chapter 3.1, these meteorological conditions induced an error on the FODS column with a maximum temperature difference of T_{PVC}= -0.265 K and T_{bare}= -0.137 K according to the energy balance model (Figure 16). The maxima come along with the highest measured value for the longwave radiation delta ΔL of -65 Wm^{-2} on the 17.02.2022

(Figure 15). The temperature difference determined by the model between the actual air temperature T_A and the measured FODS temperature T_f was negative on the 17.02.2022, consequently the FO array experienced a higher energy loss than the surrounding air. Looking at the positive deviation, the maximum error appeared on the 16.02.2022. T_{PVC} reached -0.013 K and T_{bare} equalled -0.01 K at prevailing low windspeed conditions of 1 ms^{-1} and positive longwave radiation balance of 26 Wm^{-2}.

In accordance with the correction model, the bare fiber always indicates a lower deviation to the actual air temperature, while the PVC coated fibre type shows a higher sensitivity to the influence of radiation and wind. Due to the greater diameter the spacing of the isotherms decreases steeper at the PVC, than at the bare fiber. Within the boundaries of 0.3 and 7 ms^{-1}, as well as -150 to 50 Wm^{-2}, the error of the PVC fibre is enhanced significantly compared to the bare fibre. To mention is, that the uncertainty is the highest for windspeeds near the lower boundary. Because of the larger exposed surface, the energy gain respectively loss at $\Delta L \neq 0$ Wm^{-2}, causes a steeper gradient at the PVC fibre (Figure 16). With respect to the hypothesis for this research question, the energy balance supports the thesis, that the PVC fiber has a stronger deviation from the actual air temperature than the bare fiber.
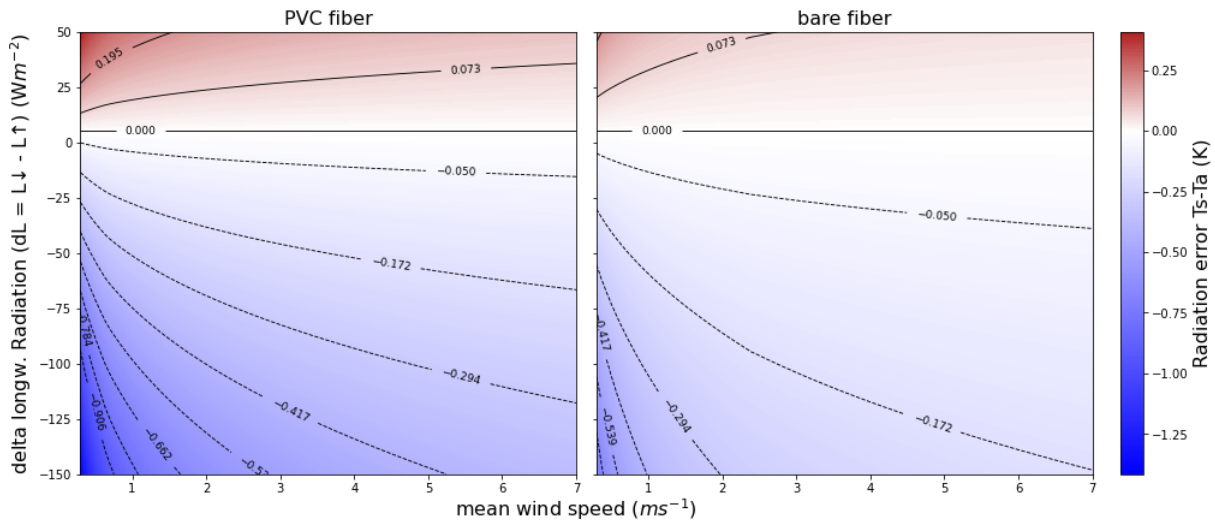

Figure 16: Radiation error T_s-T_a as a function of the main drivers: Based on the condition from the 14.02.2022 to 17.02.2022 the temperature was assumed to be constant -11.75°C. The shortwave term was neglected since the incoming shortwave irradiation never exceeded 6 Wm^{-2}. The energy loss through the longwave radiation term was assumed to be constant, while the counter radiation from the atmosphere was varied from -150 Wm^{-2} to 50 Wm^{-2}.

To observe the significance of the measurement error, the extrema of the measurement deviation were compared to the accuracy of the Silixa XT. The precision and bias of the FODS setup were determined during the NYTEFOX experiment, in combination with the same calibration devices. The accuracy of FODS temperature readings relies on data gathered from calibration baths. The bias is defined as the mean of daily averaged temperature differences between the fiber and reference (PT100) measurements in each SoPhaB. Meanwhile, the precision is determined by the median of the daily spatial σ of the fiber temperatures within each calibration bath. For the FODS measurement device from Silixa and the SoPhaBs this results in a bias of 0.03 K and a precision of 0.28 K (Zeller et al., 2021).

As a result of the taller diameter of the PVC FO cable, the probability density of the occurring temperature deviation shows a broader spectrum in the temperature (Figure 17). The histogram is based on the dataset that was recorded with both FODS columns at the 14.02.2022 to 17.02.2022.
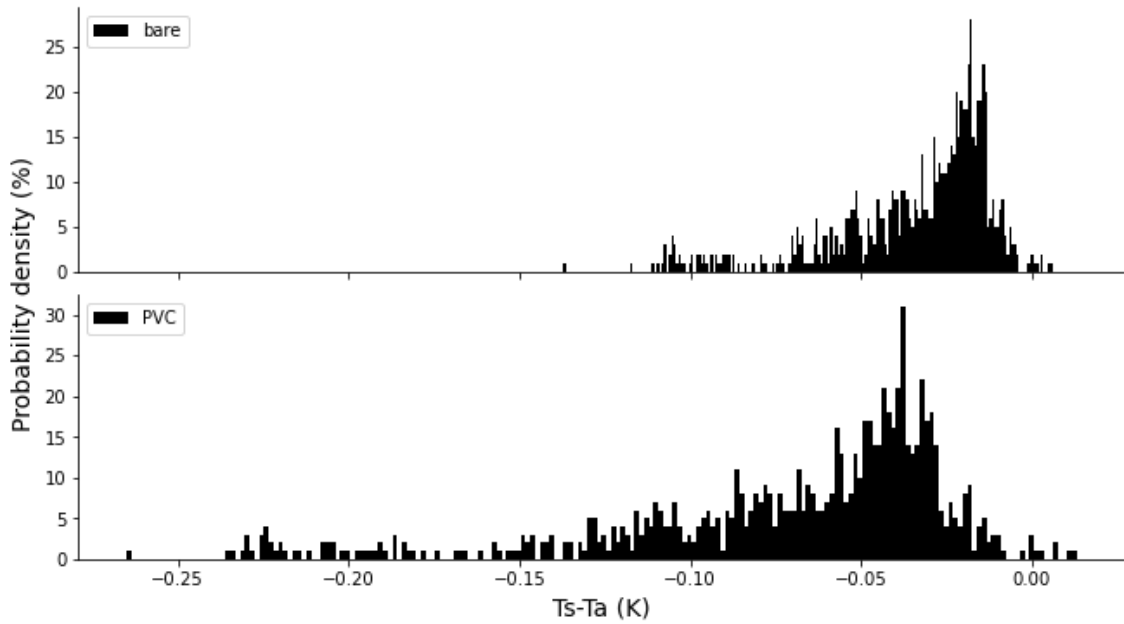
Figure 17: Histogram of the deviation between the observed FODS temperature and the dry-bulb air temperature according to the energy balance model. The upper graph shows the bare FO cable and the bottom subplot the PVC FO type. Observation time: 14.02.2022 to 17.02.2022, temporal averaging 5 min.
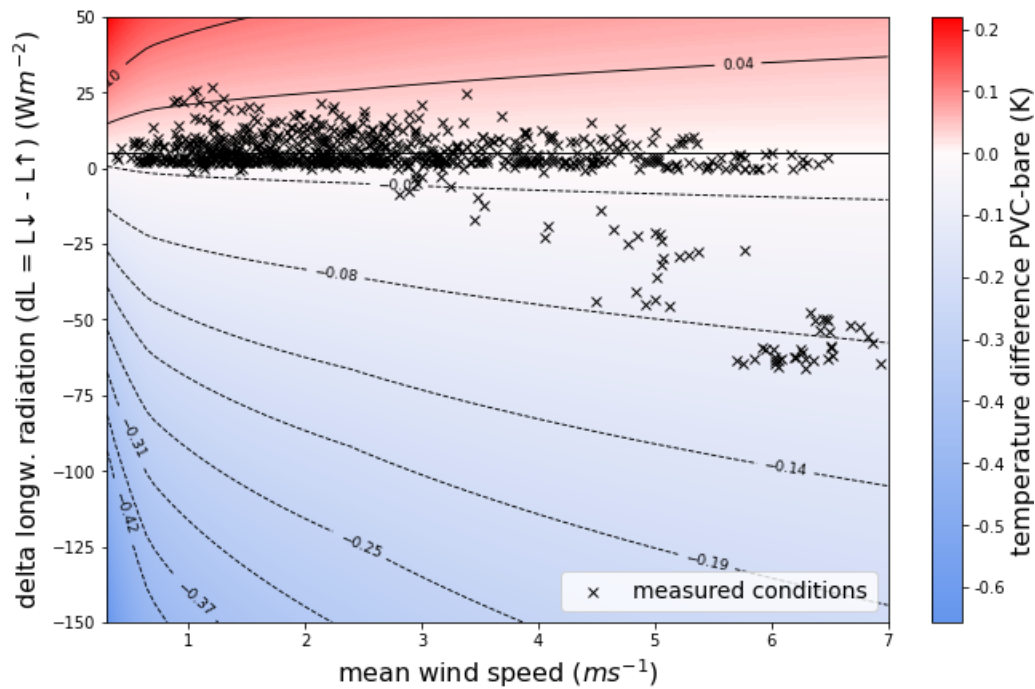

Figure 18: Comparison of temperature difference between PVC and bare FO types under the influence of the measurement errors, through longwave radiation and convection, during polar night. The error is effective, when air temperature is measured with the FODS, since the sensor is subjected to its physical environment. The x-axis shows the mean wind speed from 0.3 to 7 ms⁻¹. The longwave radiation balance is set on the y-axis. Positive values, mean an energy gain for the surface of the FO, while negative values mean energy loss for the system. The measured conditions from the 14.02.2022 to 17.02.2022 are indicated with an x. Based on the data the maximal occurred errors are -0.1 K and 0.05 K.

To answer the question of the magnitude of the difference between both FO types, the temperature deviation was calculated (Figure 18). The measured conditions during the observation are marked with x. As a result, of the uniform condition during our measurement period the shortcoming between both fiber types never exceeded the 0.1 K mark.

3.3. Heat diffusivity of the snow layer (RQ2)

The analysis for the second research questions is structured as followed: The chapter starts with an example period for the optimized alpha and in the result the spread of temperature within the snow mass. Afterward the changing over time of α during the observation period is discussed and the frequential decomposition of this signal is presented. The significance of the results is discussed, and possible error sources are revealed. Finally, this chapter tries to connect the data from the USA with the thermodynamic inside the snow cover.

One example period of the algorithm was simulated separated in four subplots with different thermodynamic properties of the snow medium (Figure 19). The subplot marked with a) shows the actual measured temperature profile. In panels b) and c) the temperature was simulated for a user-set low or high heat diffusivity at $\alpha = 10^{-8}$ m^2 s^{-1} and $\alpha = 10^{-5}$ m^2 s^{-1}. Within the graphic b) one sees that the low temperature conduction supresses the vertical exchange, while c) is characterized by temperature spikes nearly over the complete profile. Subplot d) fits the optimization problem the best and represents the lowest RMS error.
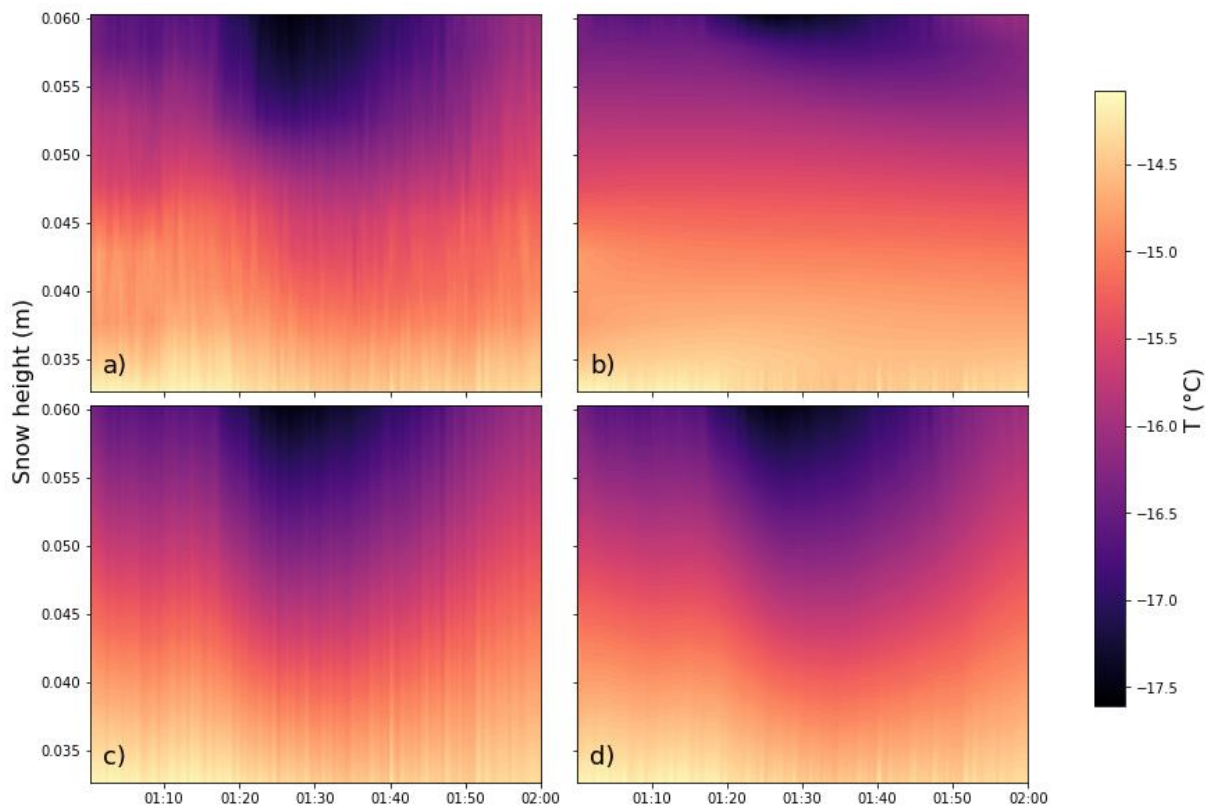

Figure 19: Exemplary visualized temperature spreads within the snow on fixed column height between 0.03 m and 0.06 m for different thermodynamic properties of the snow medium: a) measured temperature, b) simulated with low $\alpha = 10^{-8}$ m^{2}s^{-1}, c) simulated with high $\alpha = 10^{-5}$ m^{2}s^{-1}, d) optimum alpha dynamically determined by solving Equation (9) as described in Section 2.4.3. The temperatures at the upper and lower heights (0.03 m and 0.06 m) were taken as the Dirichlet BCs. The exemplary section is from the 13.02.2022. The figure with low values for alpha shows the oppressed heat conduction between the two boundaries, while a high alpha enables temperature changes from the snow surface to pass through the boundaries directly.

The changing over time of the heat diffusivity with the three differing height levels (Figure 12) for the algorithm provides insights into the similarities and differences between the data. Within the three signals determined by the algorithm similar pattern and anomalies of α occurred (Figure 20). The three datasets were compiled by the same temporal recording, however only with variable height coordinates. All provided signals, see Figure 20, show an accumulation of single α values with a high probability density. Around this accumulation the signals show also scattering with strongly differing

heat diffusivity values. Expressed in values, there are variations in the thermal diffusivity time series. The 95-percentile of the data ranges between $\alpha = 2.95 \times 10^{-6}$ m²s⁻¹ with the lower vertical profile section and 3.89×10^{-6} m²s⁻¹ on the upper vertical profile section. The fixed profile was located in between. For the 5-percentile the heat diffusivity varies between $\alpha = 2.15 \times 10^{-9}$ m²s⁻¹ at the lower vertical profile section and 2.55×10^{-9} m²s⁻¹ at the upper profile section. All three signals have a similar scattering in the signal. The complete series of the diffusivity extends over five orders of magnitude from 10^{-4} m²s⁻¹ to 10^{-9} m²s⁻¹. Based on the information provided, Figure 20 shows extreme values of thermal diffusivity and a rapid rate of change towards these extreme values. Aside from that, the series indicates a strong trend on the hourly or daily scale. The three subplots in Figure 20 all have the similar standard deviation on short time periods, due to temperature noise, falsified differencing, but also due to high-frequency variation caused by turbulence. The two-order magnitude variance in 15-minute scale may be attributed to non-diffusive heat transfer, like convection or wind pumping.
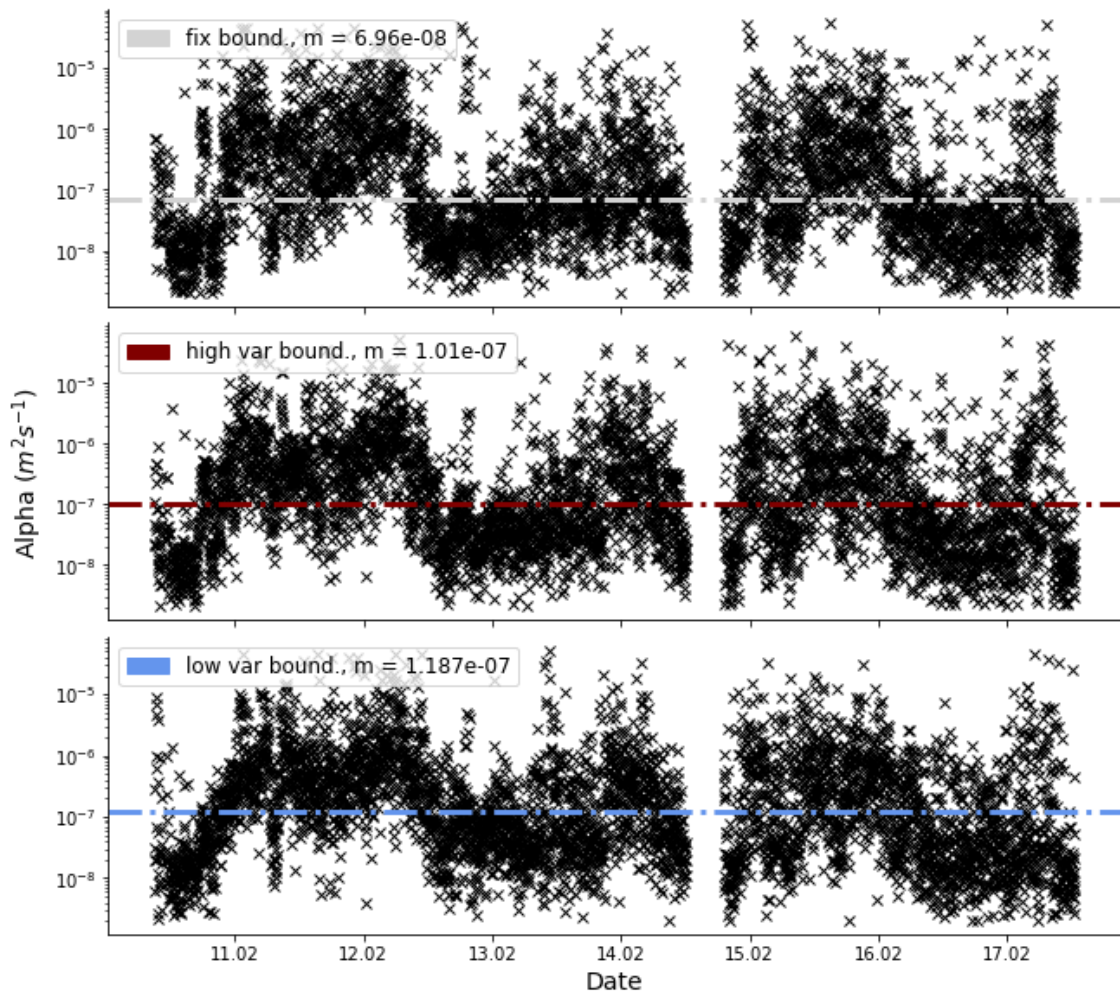

Figure 20: Results from the finite differences approach. The colouring and subplots match the snow detection chapter 2.4.2, respectively Figure 12. The heat diffusivity is given in logarithmic scale on the y-axis. The upper subplot uses the fixed boundaries, while the two lower graphs were determined with moving snow heights.

To analyse the relation between the heat diffusivity and the depth of the snow, the algorithm was executed with a vertical profile section 1cm below the detected snow surface and additional with a variable vertical profile section in 2.5cm depth below the snow surface. Recall the spatial domain of the snow volume, the three sections (Section 2.4.2) had a maximum height deviation of 10 cm after snowfall events, hence there is no major difference in the median results. A deeper variable section was not possible, due to the physical extent of the snow layer. The temporal decomposition of the original series reduced the signal to the lower frequencies and indicates the trend on the long

timescale bases, hourly respectively daily. The results of the variable upper and lower vertical profile sections show a high correlation to each other. Although the two series were calculated with BC in 1cm distance to each other, the trend indicates a slight delay and a lower diffusivity (Figure 24). Recalling the results from the snow height detection, the temperatures standard deviation increases with decreasing distance to the surface because temperatures closer to the surface experience more change in time and exhibit higher gradients.

The Bior5.5 wavelet decomposition allows for separation of coherent structure based on their temporal domain. In Figure 21 the long-term change or low frequencies of the thermodynamic property is presented for the three vertical profile sections on stage 4, i.e., it includes only structure with a critical duration D_c longer than 47 minutes. Although the median value for α does not differ significantly, the temporal change show multiple differences between the variable and the fixed vertical profile sections.
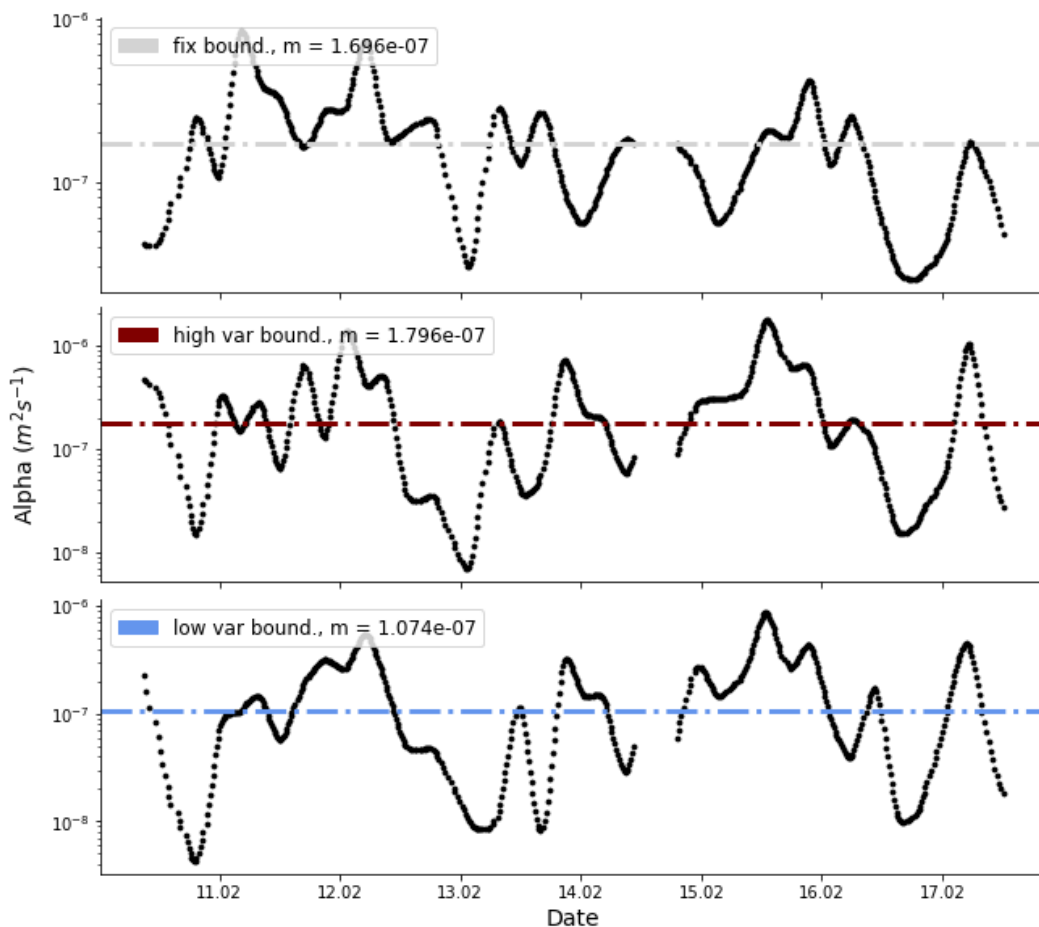

Figure 21: Low-frequency trend of the heat diffusivity obtained by temporal decomposition on 15 min averaging with the BIOR5.5 wavelet. Comparison of the results with different boundaries for the calculation. The top plot shows the values for alpha with fixed boundaries. The middle and bottom plots show the value for variable boundaries in 1cm respectively 2.5 cm below the surface. For detailed information to the heights of each vertical profile section, see capture 2.5.3. The critical event duration on the frequency decomposition was 47 min.

The fixed BC differs in the change over time in comparison to the variable BC. These may be caused by multiple aspects. Firstly, the changing snow height is not reflected in the calculation and hence the signal is subjected to changing variability of the temperature and isolation from the surface influence. Secondly, to reach such a high spatial resolution, the coiled fibre column setup was necessary. This approach assumes, that both y and x-axis, i.e., the surface parallel level, is completely homogeneous. Only if x and y coordinates of each measurement bin are neglected, the temperature can be aligned on a straight along the z-axis. But this can only be partially correct, since we have several factors,

likewise lee effects, that can cause heterogeneities. While the height difference of each variable vertical profile section was chosen with constant amount of 1 cm (4 bins equals one FO turn), the BC are aligned in the same orientation to the FO column. Only every fourth datapoint, is orientated in the same direction of the FODS column and is subjected to similar wind regime. In conclusion, the fixed and variable vertical profile sections have a limited comparability, because potential inhomogeneities within the column orientation effect the result of the diffusivity, while both variable profile sections are comparable due to the orientation on the column outside.

Assuming a completely sealed snow volume, without any influence by air flow, the theoretical limits were given by the two components of the porous medium. The heat diffusivity of ice, which is equivalent to $\alpha_{Ice} = 1 \times 10^{-6}$ m^{2}s^{-1}, defines the lower possible limit and for air the theoretical upper limit is given with $\alpha_{Air} = 2 \times 10^{-5}$ m^{2}s^{-1}. Previous research that used this assumption to validate the result of the observed signal (Reusser and Zehe, 2011). Since an imaginary snow mass is not a sealed volume, the air volume is subjected to an exchange and hence also to the transport of sensible or latent heat. For this reason, these fixed theoretical boundaries lack in meaningfulness, instead one would assume the possible range to move according to the turbulent regime over the surface.

3.3.1.   Relationship between airflow and the heat diffusivity

For the correlation analysis the data from the USA were used. In this paragraph the correlation between α and the boundary layer turbulent flow was observed exemplarily based on the TKE, but the same analysis was done with the total wind speed, the vertical wind component, and the friction velocity. Since these parameters are all highly correlated, the result is the similar and not explicitly shown. First the variation over time for TKE and α were compared against each other (Figure 22). Both subplots share the same x-axis, with the observational period. The y-axis is scaled logarithmically and the TKE was inverted for the bottom subplot. The upper subplot was plotted with the low frequency heat diffusivity on the decomposition level 2. The critical event duration D_c for this decomposition level equals 94 s.
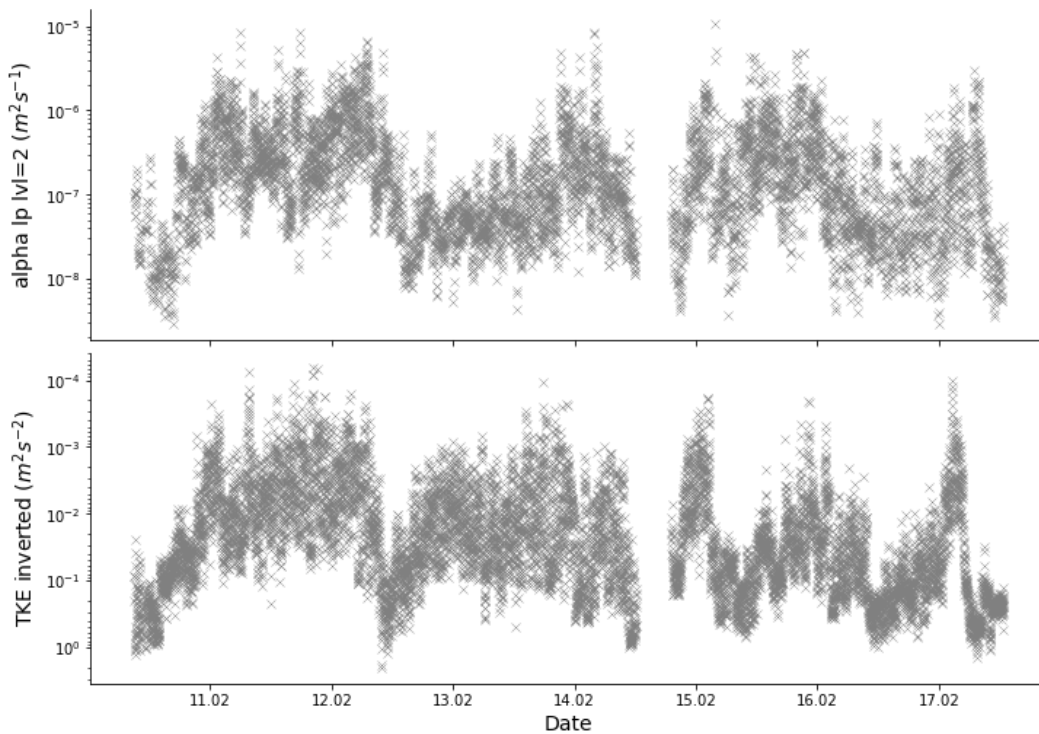

Figure 22: Correlation between heat diffusivity α with the TKE. For better visualization the scale is inverted in the bottom subplot. For the upper subplot the decomposition level 2 data of α was used. The critical event duration D_c equals 94 s.

Figure 22 indicates a connection between the two parameters. Although the variation over time shows certain similarities, there are several exceptions were the connection fails, e.g., on the 12.02.2022 at midnight the trend diverges completely, the same applies for the second half of the 15.02.2022. The background for this variating behaviour needs to be observed in further research.

For a better quantification 200 datapoints were averaged, see red line, and standard deviation σ was indicated. The bin average plot (Figure 23) shows an anticorrelation of the TKE and α on the low-frequency range after the decomposition (see 2.4.4). The differentiation in the frequency was bases on Equation (12), resulting in a critical event duration of $D_c = 188\ s$. Low pass filtered data decreases with an increasing energy in the turbulent motion. The high pass filtered signal for α suggests no correlation with the turbulent regime of the boundary layer.
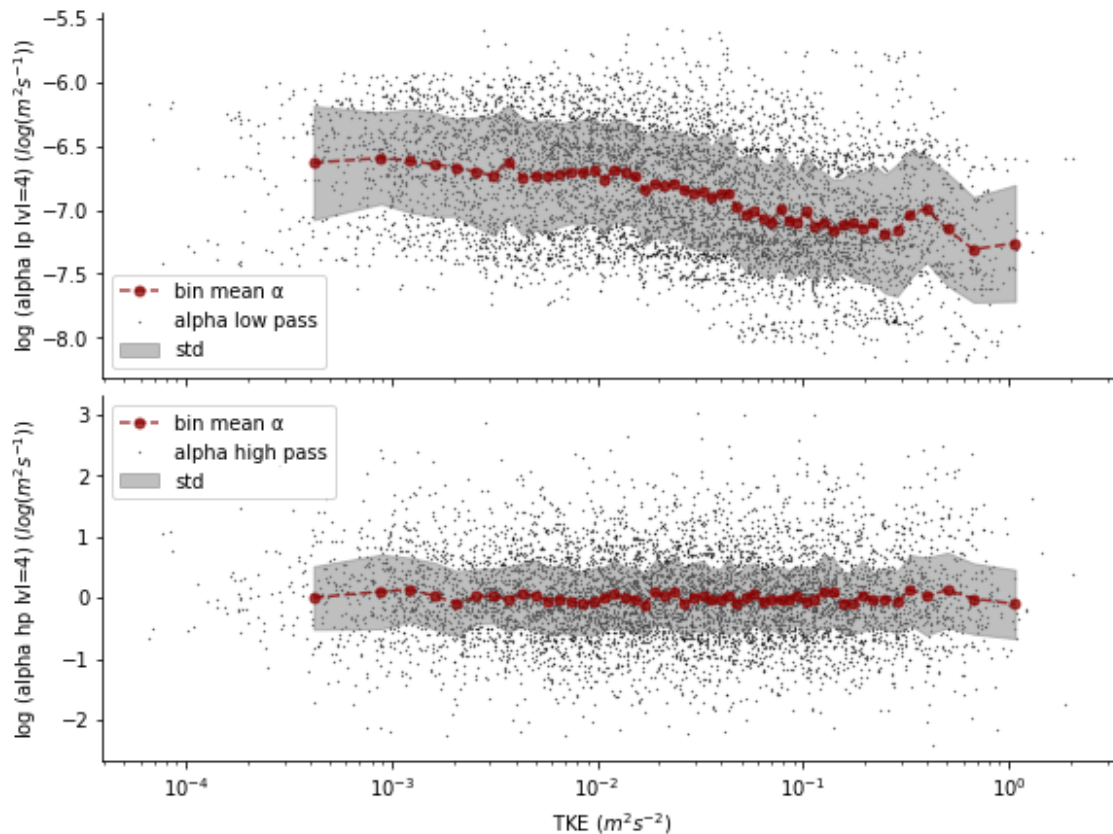

Figure 23: Bin averaged heat diffusivity separated into high and low frequencies. 200 bins have summarized to the mean. The difference of one σ from the mean trend is marked with grey background. D_c on decomposition level 4 with a $\Delta t = 60\ s$ equals 188 s.

To explain the underlying process further research needs to be done. One hypothesis observes, that with rising TKE the vertical exchange of energy is so efficient, that differencing of the spatial domain leads to a miscalculation of α. To face this issue, the vertical profile section could be expanded to improve the accuracy of the algorithm. Furthermore, flux BC, or Neumann BC, could be implemented as verification for the results of this work or as improvement of the previous procedure with Dirichlet BC. However, this dataset was observed during temperature always below -5°C, the difference using temperature BCs instead of flux conditions should not be significant. At least, improvements could also be done to the snow height detection because accumulation of snow is not pictured sufficiently. The quality of the snow height detection suffers of the effect of uneven accumulation of snow due to the dominant wind direction from south-east in the Adventdalen valley (Figure 26).

4. Conclusions

Related to the RQ1, the prominence of the radiation error was successfully determined with the energy balance model. The model did not reject the hypothesis 1. With respect to the extremely precisely bias of the Silixa XT, one can conclude, that the error on the measured air temperature is significant. Nevertheless, the prevailing conditions should be considered, since for most of the data, the error stays below this bias. Since meteorological situation during longer FODS experiments may statistically exceed the magnitude of the occurring error of this dataset, the correction may become more important. For the most accurate air temperatures with FODS, the usage of the bare fiber can be recommended and respectively or a correction could be implemented. The bare fiber has a clear advantage over the PVC fiber, because of less scattering in the temperature deviation. This decision should be made by the application of the FODS and the requirements to the sensitivity or tensile strength of the fiber.

The methodology of determination of the heat diffusivity (RQ2) was successfully adapted to the FODS data within this work and the results match the range of diffusivities found in literature. The temporal change of heat diffusivity during the observation showed a connection to the boundary layer turbulence. However, the hypothesis 2 contradicts to the result of the analysis, instead the TKE was indicated as anticorrelated to the heat diffusivity α. The high-frequency composition of alpha could not be linked with the TKE. In the conclusion three improvements can be made for future research: First, since for the application of a FODS column a single LiDAR based point measurement of the snow height is not sufficient, due to variation along the circumference of the column, a manual measured snow height could be sensible for the validation of the snow height detection. Within further analysis of the heat diffusivity, an accurate snow height detection is obligatory. Secondly, you may increase the accuracy of the numerical approach, by using the widest possible range in the vertical profile section for the algorithm. Thirdly, for different environmental conditions the use of Neumann BCs also may offer a higher precision in the results, respectively fluxes can be used as verification.

Due to the harsh conditions of the environment and cold temperatures the technical feasibility was limited for the bare optical fibre. While the tightly buffered PVC fibre withstood the cold temperature, the handling of the even more delicate bare fibre presented itself as quite difficult. In general, the routing of the fibre-optic cable needs to be done cautiously. During the installation the bare fibre broke outside the station. The damage couldn´t be repaired with the splicing tool. All the attempts to splice the fibre failed at the low temperatures. Despite this, it was possible to draw the comparison between the two types. Instead of the double ended calibration a single ended calibration was used. To ensure meaningful date, the raw temperature of the measurement device was related in the calibration process to an additional PT100 at the broken end (Hausner et al., 2011).

The FODS experiment was conducted successfully, gaining new inside into the thermodynamic of an artic snow mass, as well as into the factor of boundary layer flow, as a potential driver for the transfer between snow-air interface. In the department of meteorology this research enabled a better understanding about the influence of measuring with variating FO cable types and the associated error characteristics of those during the polar night on Svalbard.

Acknowledgments

5. References

Arnon, A., Selker, J., Lensky, N., 2014. Correcting artifacts in transition to a wound optic fiber: Example from high-resolution temperature profiling in the Dead Sea. Water Resour. Res. 50 (6), 5329–5333.

Baehr, H.D., Stephan, K., 2019. Wärme- und Stoffübertragung. Springer Berlin Heidelberg, Berlin, Heidelberg, 828 pp., DOI:10.1007/978-3-662-58441-5.

Bärwolff, G., 2020. Numerik für Ingenieure, Physiker und Informatiker. Springer Berlin Heidelberg, Berlin, Heidelberg, 426 pp., DOI:10.1007/978-3-662-61734-2.

Bejan, A., 2013. Convection heat transfer, Fourth edition ed. Wiley, Hoboken New Jersey, xxxiii, 658 pages.

DRAKE, S.A., HUWALD, H., PARLANGE, M.B., SELKER, J.S., NOLIN, A.W., HIGGINS, C.W., 2016. Attenuation of wind-induced pressure perturbations in alpine snow. J. Glaciol. 62 (234), 674–683.

Drusová, S., Bakx, W., Doornenbal, P.J., Wagterveld, R.M., Bense, V.F., Offerhaus, H.L., 2021. Comparison of three types of fiber optic sensors for temperature monitoring in a groundwater flow simulator. Sensors and Actuators A: Physical 331, 112682.

Foken, T., 2021. Springer Handbook of Atmospheric Measurements. Springer International Publishing, Cham, 1761 pp., DOI:10.1007/978-3-030-52171-4.

Freundorfer, A., Lapo, K., Schneider, J., Thomas, C.K., 2021. Distributed sensing of wind direction using fiber-optic cables. Journal of Atmospheric and Oceanic Technology.

Hartnett, J.P., Irvine, T.F. (Eds.), 1987. Advances in Heat Transfer. Elsevier.

Haugan, P.M., 1999. Structure and heat content of the West Spitsbergen Current. Polar Research 18 (2), 183–188.

Hausner, M.B., Suárez, F., Glander, K.E., van de Giesen, N., SELKER, J.S., Tyler, S.W., 2011. Calibrating single-ended fiber-optic Raman spectra distributed temperature sensing data. Sensors (Basel, Switzerland) 11 (11), 10859–10879.

Lange, M.A., 1985. Measurements of thermal parameters in Antarctic snow and firn. Annals of Glaciology 6, 100–104.

Mukherjea, K., 2002. Finite volume methods for hyperbolic problems. Cambridge University Press, Cambridge, 558 pp., DOI:10.1017/CBO9780511791253.

Oldroyd, H.J., Higgins, C.W., Huwald, H., Selker, J.S., Parlange, M.B., 2013. Thermal diffusivity of seasonal snow determined from temperature profiles. Advances in Water Resources 55, 121–130.

Reusser, D.E., Zehe, E., 2011. Low-cost monitoring of snow height and thermal properties with inexpensive temperature sensors. Hydrol. Process. 25 (12), 1841–1852.

Sayde, C., Thomas, C.K., Wagner, J., Selker, J., 2015. High-resolution wind speed measurements using actively heated fiber optics. Geophys. Res. Lett. 42 (22).

Selker, J., van de Giesen, N., Westhoff, M., Luxemburg, W., PARLANGE, M.B., 2006. Fiber optics opens window on stream dynamics. Geophys. Res. Lett. 33 (24).

Sigmund, A., Pfister, L., Sayde, C., Thomas, C.K., 2017. Quantitative analysis of the radiation error for aerial coiled-fiber-optic distributed temperature sensing deployments using reinforcing fabric as support structure. Atmos. Meas. Tech. 10 (6), 2149–2162.

Singh, V.P. (Ed.), 2011. Encyclopedia of Snow, Ice and Glaciers. Springer Netherlands, Dordrecht, Online-Ressource.

Stull, R.B. (Ed.), 1988. An introduction to boundary layer meteorology. Springer, [Berlin], 670 pp.

Sturm, M., Holmgren, J., König, M., Morris, K., 1997. The thermal conductivity of seasonal snow. J. Glaciol. 43 (143), 26–41.

Thomas, C., Foken, T., 2005. Detection of long-term coherent exchange over spruce forest using wavelet analysis. Theor. Appl. Climatol. 80 (2-4), 91–104.

Thomas, C.K., Huss, J.-M., Abdoli, M., Huttarsch, T., Schneider, J., 2022. Solid-Phase Reference Baths for Fiber-Optic Distributed Sensing. Sensors (Basel, Switzerland) 22 (11).

Thomas, C.K., Kennedy, A.M., SELKER, J.S., Moretti, A., Schroth, M.H., Smoot, A.R., Tufillaro, N.B., Zeeman, M.J., 2012. High-Resolution Fibre-Optic Temperature Sensing: A New Tool to Study the Two-Dimensional Structure of Atmospheric Surface-Layer Flow. Boundary-Layer Meteorol 142 (2), 177–192.

Thomas, C.K., Law, B.E., Irvine, J., Martin, J.G., Pettijohn, J.C., Davis, K.J., 2009. Seasonal hydrology explains interannual and seasonal variation in carbon and water exchange in a semiarid mature ponderosa pine forest in central Oregon. J. Geophys. Res. 114 (G4).

Thomas, C.K., Selker, J., 2021. Optical Fiber-Based Distributed Sensing Methods, in: , Springer Handbook of Atmospheric Measurements. Springer, Cham, pp. 609–631.

van den Broeke, M., Fettweis, X., Mölg, T., 2011. Surface Energy Balance, in: , Encyclopedia of Snow, Ice and Glaciers. Springer, Dordrecht, pp. 1112–1123.

van Rossum, G.a.D., 2015. Python reference.

Vihma, T., 2011. Atmosphere-Snow/Ice Interactions, in: , Encyclopedia of Snow, Ice and Glaciers. Springer, Dordrecht, pp. 66–75.

Wang, W., McGregor, H., Short, M., Zeng, H., 2016. Clinical utility of Raman spectroscopy: current applications and ongoing developments. AHCT, 13.

Zeller, M.-L., Huss, J.-M., Pfister, L., Lapo, K.E., Littmann, D., Schneider, J., Schulz, A., Thomas, C.K., 2021. The NY-Ålesund TurbulencE Fiber Optic eXperiment (NYTEFOX): investigating the Arctic boundary layer, Svalbard. Earth Syst. Sci. Data 13 (7), 3439–3452.

Žkauskas, A., 1987. Heat Transfer from Tubes in Crossflow, in: Hartnett, J.P., Irvine, T.F. (Eds.), Advances in Heat Transfer, vol. 18. Elsevier, pp. 87–159.
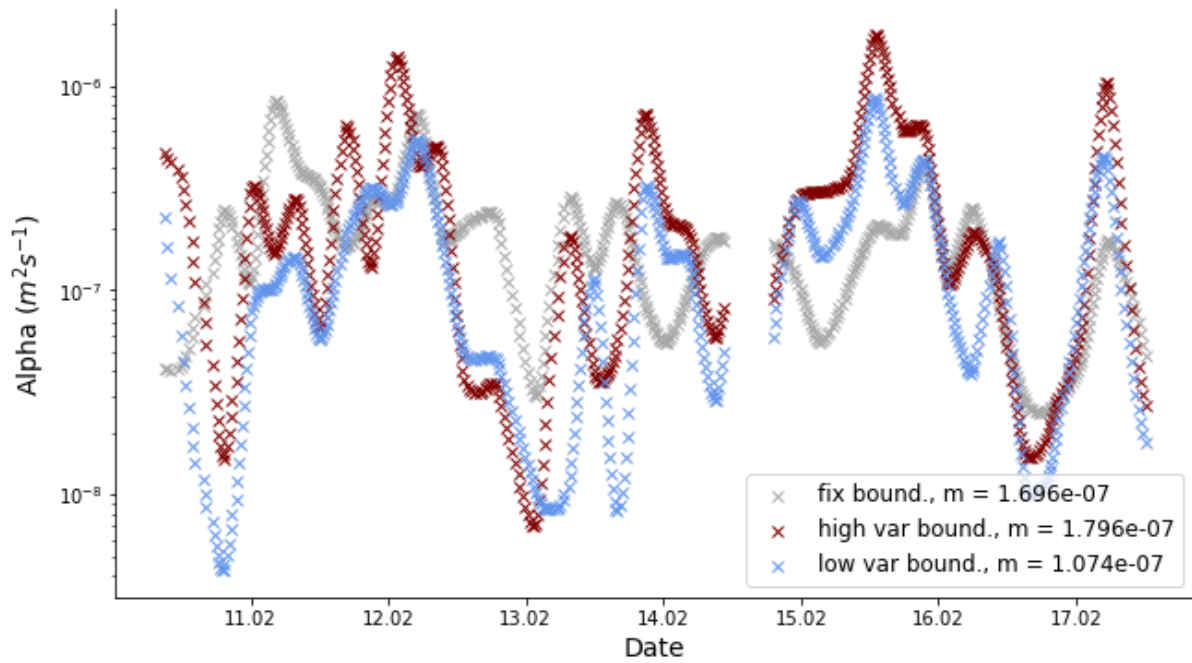
Additional figures

Figure 24: Combined low-frequency series of the three snow heights on 15-minute database decomposed with the BIOR 5.5 wavelet bibliography.
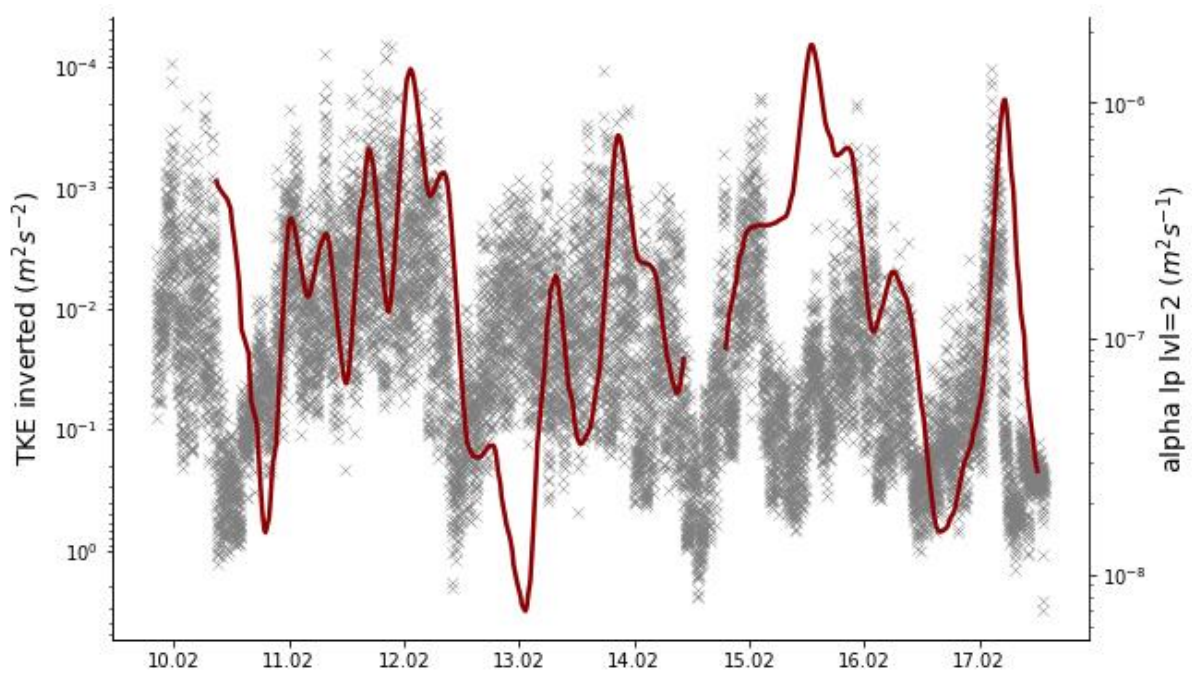

Figure 25: Trend of low-frequency decomposition of the heat diffusivity (stage 4) and the turbulent kinetic energy. The graphic emphasis the differences between both signals.
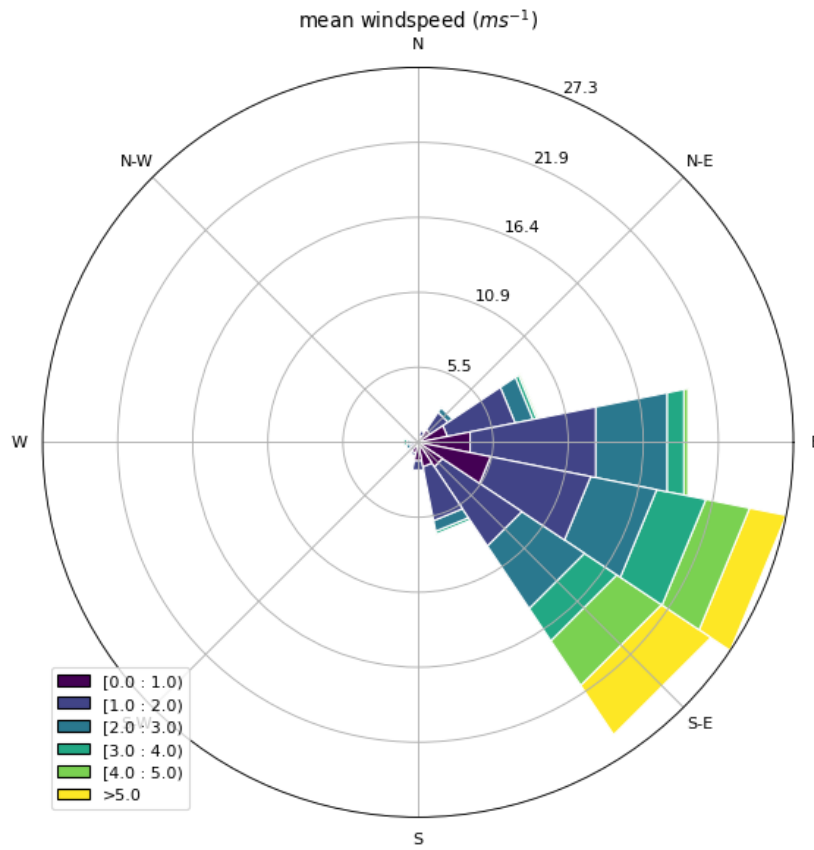
Figure 26: Distribution of the mean wind speed (ms⁻¹) presented as wind-rose plot. The plot is normed, i.e., the cumulated sum of all the bars forms 100 %. During the Measuring period: 10.02. - 17.02.2022, averaging interval of 1 min.
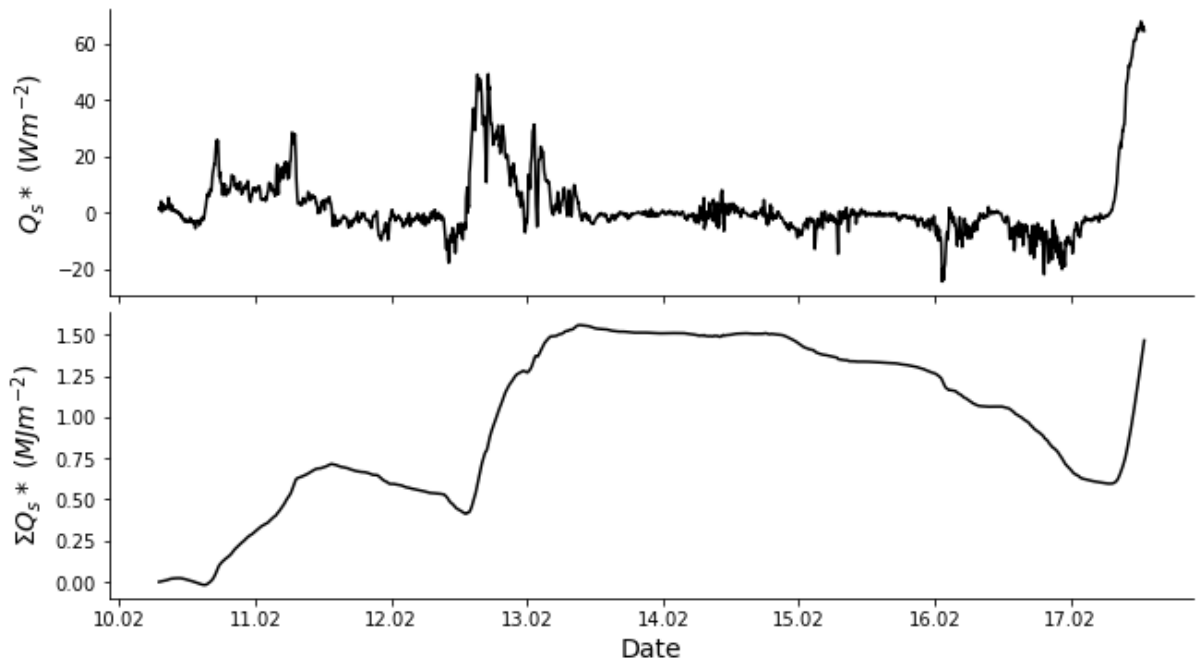

Figure 27: Radiation balance and cumulative trend of Q_s * over the observation period 10.02. - 17.02.2022. The radiation measurements provided by UNIS have a temporal resolution of 5 min. The cumulative sum is given in the unit $10^6 Jm^2$.
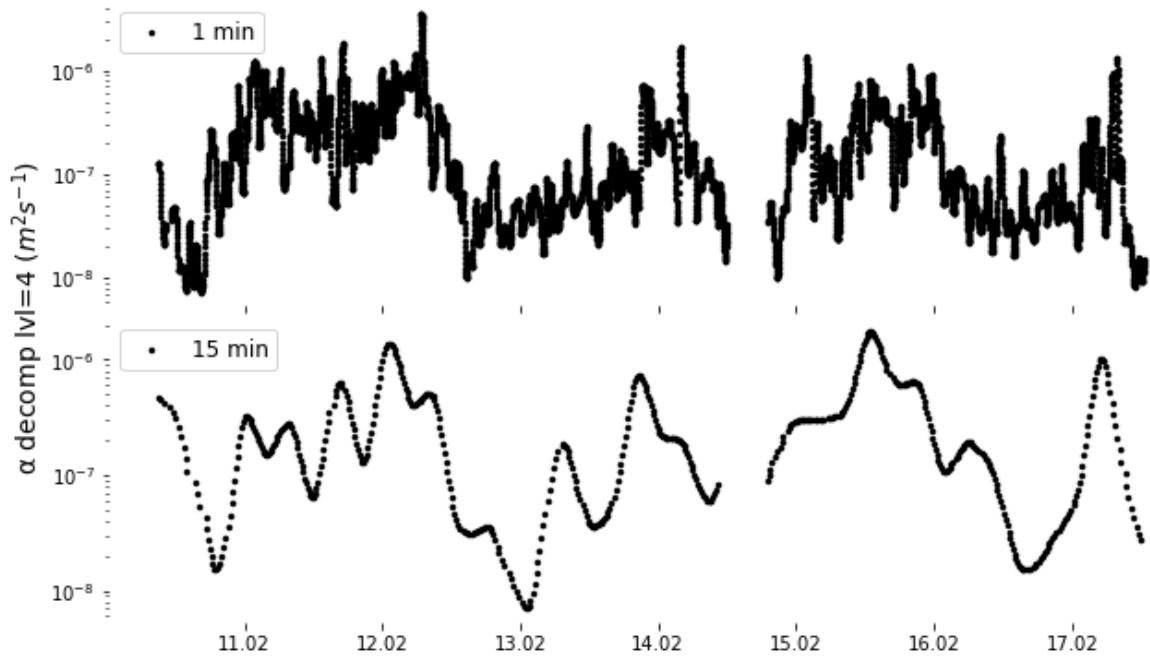
Figure 28: Low frequency decomposition of the heat diffusivity on level 4. Two subplots for the comparison of 1 min and 15 min averaging time. D_{c1}=188 s and D_{c15} =47 min.

Declaration of authorship

Hereby, I declare that I have authored the bachelor thesis,

"Investigation of the radiation error and heat transport at the snow-air interface using fibre-optic distributed sensing during the polar night in Adventdalen, Svalbard",

independently based on my own work. All direct or indirect sources used are acknowledged as

references. This thesis was not published or previously submitted to any other examination board.

14. 04. 2023

_____
Date

_____
Felix Roland Heuring